POLITECNICO DI TORINO

Master's Degree in Biomedical Engineering

Master's thesis

Transient neural interfaces: feasibility study on miniaturised and biodegradable antenna for wireless power transmission

Supervisors:

Prof. Danilo DEMARCHI

Prof. Diego GHEZZI

Candidate:

Stefania CERONE

Co-supervisors:

Eng. Adele FANELLI

Eng. Gian Luca BARBRUNI

Academic year 2022/23

Abstract

Large research in biomedical engineering is focused on implantable medical devices to allow the restoration of lost body functions. In particular, in the field of neurostimulation, implantable medical devices are usually employed to modulate the neural system as a solution to several neurological and mental diseases. In order to obtain neural activation, most of the neural interfaces require an invasive surgery for their insertion. In addition, the commonly used materials and the presence of wires usually cause a negative immunological response and thus, the need for further surgeries to replace the device. Recently, alternative methods to reach the target area of stimulation were investigated, resulting in minimally invasive implants. These improvements are focused on: i) the development of endovascular devices, able to navigate blood vessels adjacent to neural tissues following a minimally invasive angioplasty surgical procedure, and ii) the employment of transient materials which, being bioresorbable, avoid the burden of a secondary surgery. In addition, wireless power transfer systems represent an innovative and valid solution to remove wires.

This work proposes a feasibility study of an inductive power transfer system for a transient neurovascular interface with the goal of minimally invasive recording and stimulation.

Specifically, this master's thesis is focused on the design and optimisation of a two-coils inductive link. Coils' performances and coupling are derived through a full-wave simulator, replicating the implant conditions (endovascular placement, coils in magnesium and insulation in poly-ε-caprolactone). The optimal design for the coils is found by following an optimization algorithm to enhance the best performances in power delivery at the operating frequency of 40 MHz. Moreover, the final design is simulated for two different receiver coil's thicknesses, resulting from two viable fabrication methods. First, a thickness of 20 μm is used to validate a coil previously fabricated via laser cutting technique [1]. Second, a thickness of 1 μm is used to validate an alternative fabrication method, by evaporation. The former resulted in a power

transfer efficiency of 0,24% and a power delivered to the load of 1,21 mW and the latter in 0,012% and 0,061 mW, respectively.

In conclusion, probably due to the larger thickness compatible with the fabrication method, the laser-cutted coil offers stronger potential for a wireless endovascular prosthesis. In addition, in preliminary tests, the evaporation-based fabrication method proved more technically challenging than laser cutting. However, further works are needed to experimentally validate these results.

Sommario

Un’ampia ricerca nel campo dell'ingegneria biomedica è focalizzata sui dispositivi medici impiantabili per consentire il ripristino delle funzioni corporee perse. In particolare, nel campo della neurostimolazione, questi dispositivi sono solitamente impiegati per modulare il sistema neurale come soluzione a diverse malattie neurologiche e mentali. Per ottenere l'attivazione neurale, la maggior parte delle interfacce neurali richiede un intervento chirurgico invasivo per il loro inserimento. Inoltre, i materiali comunemente utilizzati e la presenza di cavi causano solitamente una risposta immunologica negativa e, quindi, la necessità di ulteriori interventi chirurgici per sostituire il dispositivo. Recentemente sono stati studiati metodi alternativi per raggiungere l'area target di stimolazione, che hanno portato alla realizzazione di impianti minimamente invasivi. Questi miglioramenti sono incentrati su: i) lo sviluppo di dispositivi endovascolari, in grado di navigare nei vasi sanguigni adiacenti ai tessuti neurali a seguito di una procedura chirurgica di angioplastica minimamente invasiva, e ii) l'impiego di materiali transitori che, essendo bioriassorbibili, evitano l'onere di un secondo intervento chirurgico. Inoltre, i sistemi di trasferimento di potenza wireless rappresentano una soluzione innovativa e valida per eliminare i cavi.

Questo lavoro propone uno studio di fattibilità di un sistema di trasferimento di potenza induttivo per un'interfaccia neurovascolare transitoria con l'obiettivo di registrare e stimolare in modo minimamente invasivo.

Nello specifico, questa tesi di laurea magistrale è incentrata sulla progettazione e l'ottimizzazione di un collegamento induttivo a due coils. Le prestazioni e l'accoppiamento dei coils sono state studiate attraverso un simulatore, replicando le condizioni di impianto (posizionamento endovascolare, coil in magnesio e isolamento in poli-ε-caprolattone). Il design ottimale per i coils è stato trovato seguendo un algoritmo di ottimizzazione per ottenere le migliori prestazioni in termini di erogazione di potenza alla frequenza operativa di 40 MHz. Inoltre, il design finale è stato simulato per due diversi spessori del coil ricevente, risultanti da due metodi di fabbricazione possibili. In

primo luogo, è stato utilizzato uno spessore di 20 μm per convalidare un coil precedentemente fabbricato con la tecnica del laser cutter [1]. In secondo luogo, è stato utilizzato uno spessore di 1 μm per convalidare un metodo di fabbricazione alternativo, mediante evaporazione. Il primo ha prodotto un'efficienza di trasferimento della potenza dello 0,24% e una potenza erogata al carico di 1,21 mW, mentre il secondo ha prodotto rispettivamente lo 0,012% e 0,061 mW.

In conclusione, probabilmente grazie allo spessore maggiore compatibile con il metodo di fabbricazione, il coil ottenuto tramite taglio laser offre un potenziale maggiore per la realizzazione di una protesi endovascolare wireless. Inoltre, nei test preliminari, il metodo di fabbricazione basato sull'evaporazione si è dimostrato tecnicamente più impegnativo del taglio laser. Tuttavia, sono necessari ulteriori lavori per convalidare sperimentalmente questi risultati.

Contents

List of Figures

1. Introduction

Several research activities in biomedical engineering are focused on the development of implantable medical devices (IMDs) and all the aspects concerning the improvement in the development process and exploitability.

1.1 Neural interfaces - devices and therapies

Neural interfaces (NIs) are devices able to interact with our nervous system in order to monitor and modulate neural activity. The advancement of this technology has seen a dramatic growth over the past decade. This is because these neurotechnologies represent a valid alternative to the development of nonpharmacological treatments for neurological disorders or to monitor and restore lost body functions. In order to obtain the stimulation, the most used means is by electrical impulses since biological tissues that are constituted of neurons or innervated by nerves naturally communicate through them. [2]

Concerning the structure of a NI, NIs implants range from devices that are placed inside the body (implanted neural interfaces, INIs) to non-invasive wearable technologies placed outside of the body for the restoration of mobility, vision, speech, balance or mood [3] Normally, these devices consist of an insulating material with specific geometric features able to interact with the targeted tissue and one or more conductive materials that carry the electrical impulses for the stimulation or the recording of signals.

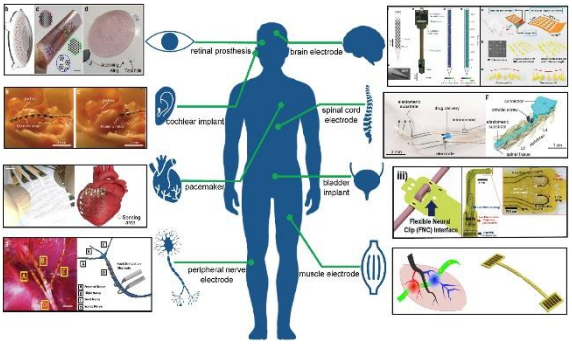

Figure 1.1: Several applications and design of neural interfaces [4]

1.1.1 Implanted neural interfaces in clinical use

Depending on the intended use of the device and its target tissue, the neural interface will accommodate different preferences, requirements, and limitations in terms of design and structure, as shown in Fig. 1.2, for the example of brain interfaces.

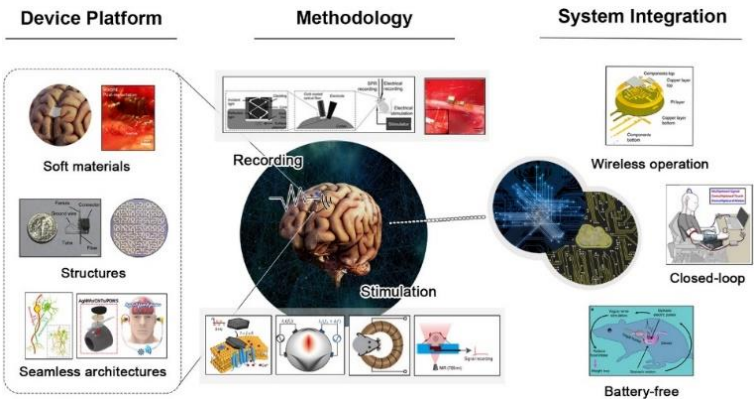

Figure 1.2: Design of different INIs [5]

Based on the aim of the INI, it can be called a *stimulator*, if its function is to electrically stimulate the neural tissue to regulate or normalize the neural activity, or neuroprosthesis, if its goal is to perform or restore a lost or impaired sensory function. [2]

Among the most relevant devices in clinical and research fields there are:

- Dep brain stimulator:
  the stimulating electrodes are designed to reach and stimulate deep structures of the brain. It was originally approved by the Food and Drug Administration (FDA)

for the treatment of movement disorders symptoms due to diseases such as Parkinson's or essential tremor; recently it has been also studied to treat other pathological conditions such as epilepsy, chronic pain, depression and mental disorders;

- Spinal cord stimulator for pain:
  through epidural stimulating electrodes, this device is able to treat hundreds of thousands of patients from chronic pain, avoiding the use of other pain relievers such as pharmaceutical drugs and opioid;

- Epilepsy Monitoring and Suppression Systems:
  several devices have been developed to reduce seizures. A clinically available solution consists of the vagus nerve stimulator (VNS). Moreover, the newest devices are able to detect the area of abnormal neural activity and trigger the stimulation to disrupt the electrical activity before it spreads and causes a clinical seizure

- Auditory prosthesis:
  cochlear implants are the earliest and the most successful INIs, they consist of an external microphone to sense the sound that is then converted into electrical impulses and transmitted to the auditory nerve, and subsequently to the brain. The first commercial device was approved by the US FDA in 1984.

- Visual prosthesis (research):
  attempt to capture and transmit visual data to the brain by capturing externally images and transmitting them by electrical impulses to the brain (as cochlear implants transmit acoustic data). Visual prostheses are not commercially available, but progress is being made in clinical investigations.

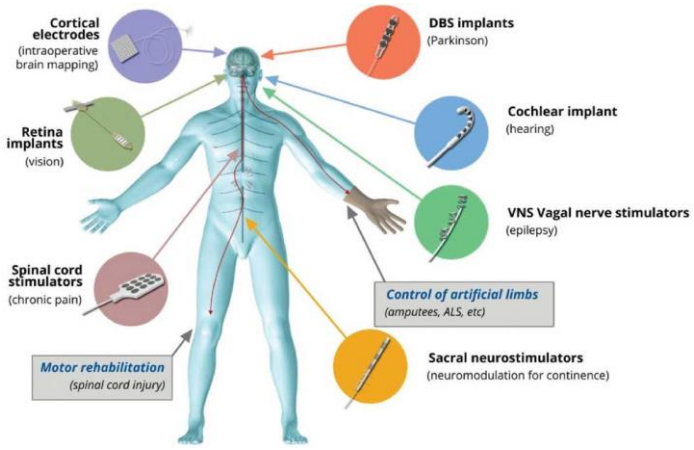

Figure 1.3:Schematics of the actual devices in clinics and research phase [6]

In general, implantable neural interfaces are very versatile and can meet the patient's needs, seeking to benefit and improve quality of life.

Despite their advantages, implantable neural interfaces also present some drawbacks:

- Invasive surgery for the insertion: most implantable neural interfaces require a rather invasive surgery such as craniotomy which potentially reduces the pool of eligible patients and cause strong inflammatory reaction.
- Secondary surgery for removal of the implants: commercially available INIs are made of abiotic materials which can cause immunological reaction and need to be removed from the body[7].
- The presence of batteries or external wires connecting the stimulating-recording electrodes to the power supply: wires are prone to cause infections and immunological responses in patients' body.

1.2 Endovascular devices

In developing new implanted neural interfaces, researchers seek to overcome the limitations discussed in the previous paragraph by identifying possible solutions. The development of endovascular devices (EDs) in the field of neurotechnology represent a solution to obtain a less invasive surgery in the insertion of INIs. Being able to navigate blood vessels and to treat adjacent target tissues from within the vessel, they can be used as an alternative technique for neural recording and stimulation.

Endovascular design in clinical use was initially studied and applied on non-electrically active devices. One of the first applications of endovascular devices was to treat conditions such as ischemic stroke, by placing an endovascular device to ensure the appropriate blood flow. In the early field of neurotechnology, these devices consisted of a singular guidewire with a sensitive tip which, once inserted inside the vessels, had the purpose of capturing the amplitude of signals from the brain such as somatosensory evoked potentials [8] or to improve the detection of epileptic foci thanks to the privileged position with respect to an external recording.[9]

Endovascular monitoring and stimulation devices have evolved significantly. Thanks to the technological advancement with the consequent miniaturization of electrode arrays and long-term implantable devices, the major limitations of the early devices, related to the presence of artifacts, unstable signal recordings, limited duration of recording, limited spatial resolution and available targets, were overcome and allowed the employment of endovascular electrical recordings.

Over the years, this class of devices was found to be highly beneficial in terms of minimal invasiveness and efficacy, opening their applications to different therapies that might benefit from an endovascular approach, such as endovascular neural interfaces for brain stimulation [10].

In particular, the use of endovascular devices in the field of neural interfaces allows the stimulation of the nervous system from the inside of a blood vessel, without the need for open brain surgery. Making the surgery for the insertion less invasive, as an ordinary angioplasty surgery, allows to increase the pool of eligible patients and reduce risks of device failure due to strong inflammatory reaction.

One of the most renowned neurovascular devices is the Stentrode™, an expandable electrode array on an endovascular stent that can be implanted via the jugular vein and advanced into the brain.

Developed by Synchron, which has already demonstrated the device validity in clinical trials, the probe was designed for recording neural signals and, by wirelessly transferring the analysed results to a computer, it has been used in humans to facilitate activities of daily living (ADLs).

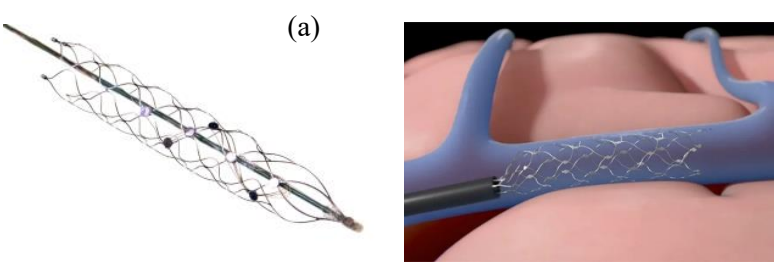

Figure 1.4: Stentrode design (a) and implantation site (b) [11]

For this kind of devices, it is reasonably crucial to choose and plan the design and the materials to be used to improve the usability and the implantation inside the blood vessel. In the case of the Stentrode™, one of the drawbacks of its employment is the metallic scaffold. Indeed, its incorporation into the walls of blood vessel for long period implantations could cause neointimal proliferation into the stent, which can lead to stenosis and occlusion of the blood vessels[12]. In order to avoid this type of situation, which would then lead to infection and thus the need for a second surgery to remove the implant, the introduction of bioresorbable materials can be considered as a possible alternative. On this path, recently, thanks to the extensive study of materials, it has been developed a transient stent-inspired neurovascular interface device [13] whose structure consists of poly-ε-caprolactone (PCL), a synthetic polyester with a long degradation time, and whose active elements are composed of poly(3,4-ethylenedioxythiophene):polystyrene sulfonate (PEDOT:PSS), thank to which the device results to be polymeric in all components and providing further promising results.

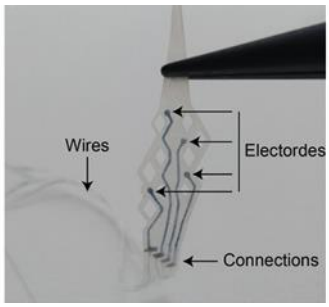

Figure 1.5: Transient neurovascular interface after fabrication [13]

1.3 Transient electronic

The technology referred to as “transient electronic” identifies every device developed with a specific class of materials, bioresorbable materials, able to physically or chemically dissolve, disintegrate, and degrade harmlessly in an environment. Such characteristic has paved a way toward environmentally degradable eco-devices with minimal or zero waste and offers the possibility to develop devices for several electronic applications.[14]

The employment of these materials has become more and more appealing for medical applications like neurotechnology. Introducing transient medical implants allows to avoid complication inherent in long term implantable devices (chronic foreign body reaction, infections and transplant rejection) and would bypass the burden of a secondary surgery for the device extraction not requiring secondary removal surgery.[15]

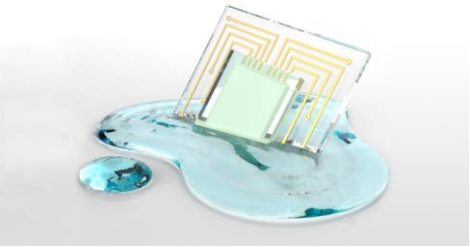

Figure 1.6: Simplified drawing of a transient process on a device [16]

Devices tailored for biomedical applications require employment of materials able to be metabolized or resorbed by the body, through safe and complete degradation by corrosion, dissolution, or hydrolysis. [17]

A typical device presents active components (sensors, electrodes, traces and connections) and insulating carriers (or encapsulation layers).

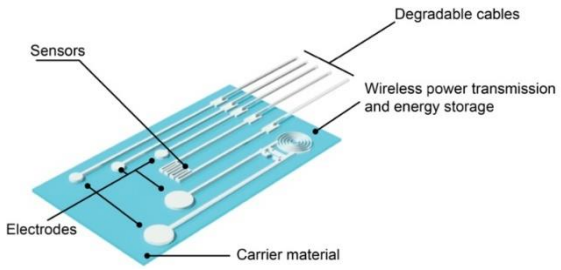

Figure 1.7: Scheme of components of a typical transient device [18]

Table 1.1 illustrates the most used materials for these parts. In the case of transient devices, all or the majority of these components should be biodegradable.

The substrate and the encapsulation ('Carrier materials') are usually made of natural and synthetic polymers which offer tuneable mechanical properties and good insulation. Conversely, metallic-based conductors such as magnesium (Mg), zinc (Zn) and molybdenum (Mo) are typically used for functional elements ('Active materials'). In particular, they are often used, as they are also conveniently involved in biological functions and are completely soluble.

Active materials	Carrier materials
•**Conductors**: Mg, Mo, Zn, Fe, W •**Semiconductors**: ZnO, Si NMs •**Conjugated polymers**: Py-*g*-PCL, PEDOT-*co*-PDLLA •**Dielectrics**: SiO_2, MoO_x, MgO	•**Natural:** silk, cellulose, natural wax, chitosan •**Synthetic**: PCL, POC, PVA, PLGA, PLLA, polyanhydrides

Table 1.1: Employed material for the development of transient devices [18]

Because of this multi-layer structure, the transient process follows two steps: the first one is the degradation of the encapsulation, the second step is the dissolution/disintegration of the functional elements.

Nowadays, the challenges in this field concern the limited compatibility of these materials with standard microfabrication processes and the alignment of the materials degradation rate, with the required device lifetime. The latter is linked to the fast degradation of materials employed as active elements**,** that researchers try to overcome by choosing and modulating the encapsulating layer materials or by trying to find different and innovative materials. [18]

1.4 Main project overview

The master thesis project wants to be an integration for an existing project, but actually propose an innovative solution for all implantable neural interfaces. The main project concerns the development of a transient neurovascular interface for neural recording and stimulation developed by Fanelli et al[13].

Specifically, this neural interface is among the most innovative and valuable in terms of overcoming the limitations of current neural interfaces, as it succeeds in solving two of the present limitations. In order to avoid the invasiveness of the implantation procedure, the solution taken is to use the vasculature as access to the neural tissues by developing a minimally invasive design to ensure an endovascular approach. In addition, the use of transient materials allows for removing the need for additional surgeries to replace the device and reduce chronic inflammatory response. In using transient materials for its fabrication, the neural interface in question also aimed to overcome limitations of these materials that include limited durability and poor compatibility with microfabrication techniques. The choice of new materials led to the development of an all-polymeric neural interface consisting of substrate and encapsulation in polycaprolactone, biodegradable polyester with a very slow degradation rate and electrodes in PEDOT:PSS with EG to improve conductivity. The semiconducting polymer is chosen for its versatility in being patternable without photolithography (developed by replica moulding) and good resistance to bending which will be needed for the endovascular design.

As mentioned then, this device has many innovations to achieve the goal of low invasiveness although it still presents connections to deliver power with cables that could provoke immunological reactions and infections.

Recently, these solutions, as seen in the previous sections, are employed in the research concerning INIs focusing on developing new minimally invasive devices able to overcome the most common drawbacks of a typical implantable devices:

- Invasive surgery for the insertion [19]: cerebrovascular system can be exploited as an access route to the neural tissue avoiding the need for invasive surgeries. This allows for interaction with the neural tissue from within blood vessels. Developing a stent electrode array overcame surgery issues since a neurovascular interface does not require craniotomies; instead, endovascular procedures minimally invasive and present a shorter recovery times. Moreover, by reducing the risks typically associated with the surgery, an increased number of patients are willing to accept the treatment.

- Secondary surgery for removal of the implants [20]: a transient device it is designed to degrade over time, avoiding the need for additional surgeries to remove or replace the device. Transient bioelectronics has been already exploited in neurotechnology. Unfortunately, some of them present limited lifetime preventing their use for mid and long-term applications. New strategies have been exploited to overcome this problem such as developing fully polymeric transient neurovascular interfaces.

Overall, the developed neurovascular interface combines two advantages: the benefits of transient bioelectronics and stent technology to allow for a wider range of applications for neural interfaces.

However, as mentioned, there is still a last drawback in current INI project that can be addressed:

- The presence of batteries or external wires connecting the stimulating-recording electrodes to the power supply: this situation gives potential way for infections and immunological responses in patients 'body. A valid solution is represented by wireless power transfer (WPT) techniques being an effective way to avoid the presence of batteries and transcranial transcutaneous wires of implantable devices. [13]

To this reason it was decided to develop a feasibility study on a WPT system to be integrated to this neural interface as a potential solution to overcome this drawback. It will be able to wirelessly deliver a stimulating impulse to the brain tissue around the implant site considered for the current neural interface (Superior sagittal sinus (SSS)).

In particular, the focus is on the design and development of the antenna, the implantable and transient part of the system. The master thesis project is therefore developed in several steps

- Creation of a complete simulation model to study the WPT system
- Fabrication of the device to experimentally validate the model

1.4.1 Wireless power transfer (WPT)

The traditional approach of supplying power to IMDs is through implantable batteries and percutaneous links. However, they are susceptible to limited energy storage, life span and to infection problems.[21]

Wireless power transfer has the potential to eliminate wires and batteries,[22] and so it has been used for applications wherever conventional wires are inconvenient as in biomedical implants.[23]

The growth in the market of WPT has seen a rapid ascent since 2012 when the development of this technology started, although it comprised almost completely of customer applications. Through the years this market is still dominated by consumers but is open to expand to the industrial and automotive markets[24]

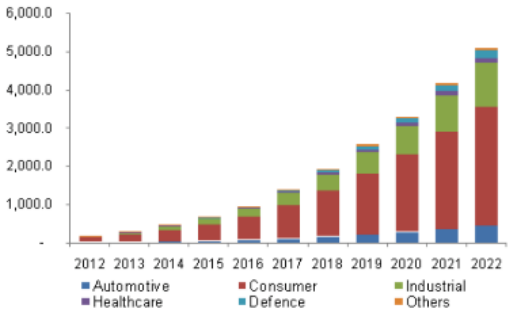

Figure 1.8: Market trend for Wireless power transfer system [24]

In general, a WPT system consists of a "transmitter" device connected to a power source, as a main line power supply, and one (or more) "receiver" device that, converting the delivered power into electric current, make it available for an electrical load. [25]

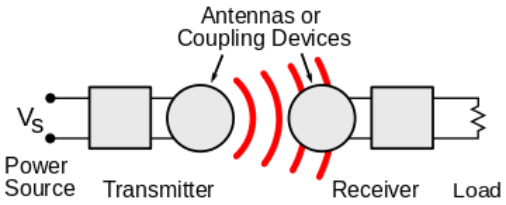

Figure 1.9: Simple block diagram of a wireless power system [22]

As shown in Fig. 1.10, in the case of inductive power transfer (IPT) the coupling elements are coils, for capacitive power transfer (CPT) are metal plates, acoustic piezo transducers for a WPT using ultrasonic waves and so forth.

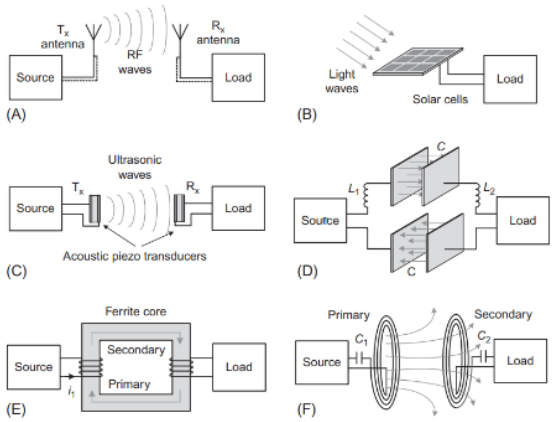

Figure 1.10: Several methods of wireless power transfer.[26]

Regarding the development of these systems for implanted neurostimulators, the technological challenge is to achieve the miniaturisation of the implantable device to allow safe surgical implantation and long-term tolerability ensuring the required power supply.[27]

1.4.1.1 Wireless transient devices

Wireless power systems have been explored, as detailed in the previous section, for various fields and applications, including the biomedical field which has tried to exploit this technology to improve and overcome the limitations of biomedical implants. The employment of wireless power supply is an interesting approach in IMDs where cables are a possible cause of infection.

Furthermore, in the biomedical field, for the reasons seen above, bioresorbable materials and transient electronics are proving to be an increasingly viable and effective solution to overcome the costs and risks associated with secondary surgical extraction.

In this regard, given new developments in the study of materials and the perspective in wireless power transfer systems, there is an increasing focus on these fields.

These aims in particular, have motivated several of John A. Rogers' work and research in the studies of transient materials soluble in biofluids in order to develop bioresorbable electronic implants and environmentally dissolvable sensors. The materials used for these studies mostly differ from those generally used in wireless systems (the most commonly used is copper) since they focus on integrating the transient characteristic to be safely implantable. The focus is on materials such as zinc oxide (ZnO), magnesium (Mg), magnesium oxide (MgO), and silk to characterise the materials and make them exploitable for use in the clinical field[28].

One of the latest works also attempts to combine the advantages of transient and wireless systems, focusing on the development of a type of bioresorbable system for wireless power transfer[29]. Specifically, this system is based on magnetic coupling between a rotating magnet as the transmitter and a bioresorbable antenna as receiver. The latter consists of two Mg coils of 10 mm diameter connected with a poly (lactic-co-glycolic acid) (PLGA) layer as a dielectric interlayer.

The wireless and transient characteristics of this design manage to overcome the limitations of many biomedical implants and is a viable solution for power supply options.

For the realisation of the bioresorbable antenna within the proposed thesis project, Rogers' literature was the basis, attempting to miniaturise the system to make it usable for the current main project's design. It was therefore decided to use a miniaturised magnesium coil

encapsulated in PCL layers as the antenna of the system, presenting itself as a transient wireless power transfer system with valid opportunities.

1.4.2 Master thesis outlines

The master thesis project is a feasibility study about the development of a miniaturized and biodegradable inductive power transfer system (IPT) for transient neural interfaces.

The latter is composed by three elements:

- Receiver coil: which generates a current proportional to the variation of magnetic flux that flows through it.
- capacitor: which works as a frequency-matching element
- diode: which rectifies the generated signal

Specifically, the thesis project is focused on the design and optimization of the inductive link between the transmitter and the receiver coil. The link between the two coils is crucial to control and allow the appropriate delivery of power in the device.

The aim is to create a complete simulation model in order to optimise the inductive coupling: coils design and properties have been simulated in a full-wave simulator (ANSYS HFSS) and the final coils' design has been chosen following steps of an optimization algorithm to enhance the performances in power delivery for a chosen operating frequency.

Moreover, a novel fabrication method, by evaporation, was preliminarily tested.

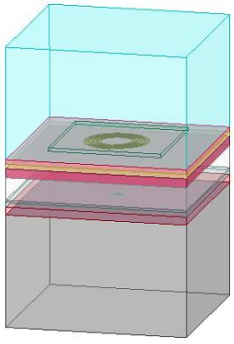

Figure 1.11: Final simulation set up

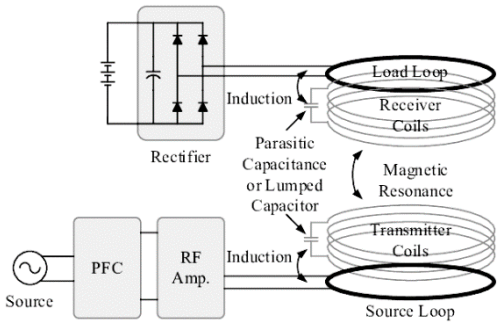

Figure 1.12:Scheme of an IPT system

2. Inductive power system: theory and applications

One of the most common WPT methods is through inductive coupling. Inductive power transfer (IPT) is based on electromagnetic induction between two mutually coupled coils [30].

Specifically, an alternating current (AC) is applied to the transmitter coil (Tx) and generates an oscillating magnetic field (B) by Ampere's law. Passing through the receiving coil (Rx), the magnetic field induces an alternating electromagnetic field (EMF) by Faraday's law of induction and generates an alternating current in the receiver [31]. At this point the induced alternating current may be rectified to direct current (DC) by a rectifier in the receiver circuit which drives the load.

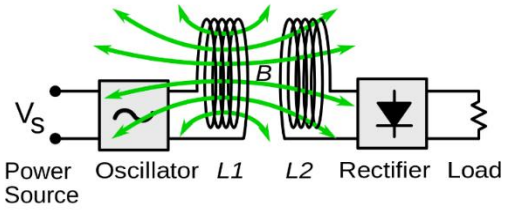

Figure 2.1: General scheme of an IPT system

Using radio frequencies (RFs) in the near-field region (operating frequencies from a few kHz to a few GHz), IPT is the most commonly used WPT approach in implantable medical devices, since RF is less attenuated by the human tissues. For this class of devices, the Tx circuit is linked to an external power source and the Rx circuit is implanted as well as the device. As result, in these cases, in between the Tx and the Rx will present the body tissues that will interfere with the mutual coupling of the coils.[21]

2.1 Circuit elements

The equivalent circuit for an IPT system is described in Fig. 2.2

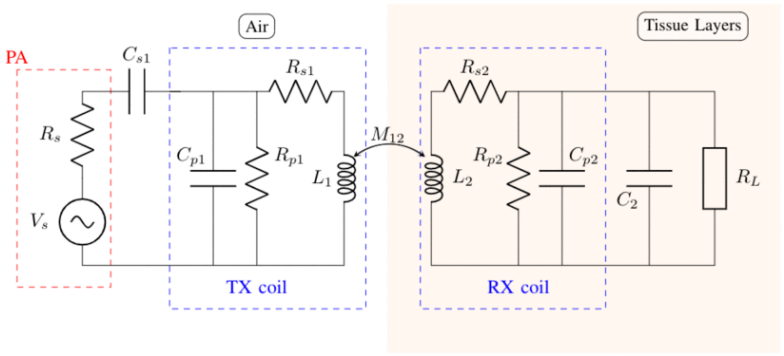

Figure 2.2: Equivalent IPT circuit [27]

in the figure is possible to individuate:

- Coil 1 (Tx coil) and Coil 2 (Rx coil): the physical Tx and Rx coils
- L_1 and L_2: self-inductance of the Tx and Rx, respectively
- Rs_1 and Rs_2: series parasitic resistances
- Rp_1 and Rp_2: parallel parasitic resistances
- Cp_1 and Cp_2: parallel parasitic capacitances
- Cs_1 and C_2: matching capacitances
- Vs: voltage source generator
- Rs: intrinsic resistance of voltage generator
- R_L: load resistance

2.1.1 Coils' geometry

The main elements of an IPT are the transmitter and receiver coils. Being the elements that exchange the power, it is important to look for a magnetic coupling between them that is optimal to obtain a higher value of power exchanged.

An important parameter is the geometry of the coils for which there are multiple alternatives (Fig. 2.3) according to applications and needs

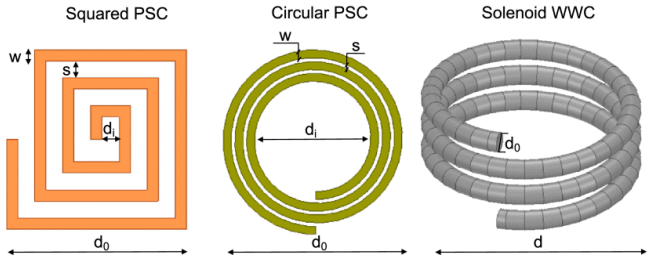

Figure 2.3: Coil design (from left to right): squared printed spiral coil, circular printed spiral coil, and solenoid wire wound coil [27]

A first division concerning the geometry is between the printed spiral coils (PSCs) and wire wounded coils (WWCs).

In micro and nano applications, PSCs are more easily fabricated but usually have lower electromagnetic properties, as the Q factor.

Adjustable geometric parameters in the design of the coils are:

For the type of coil PSC

- n: number of turns
- d_o: outer diameter
- d_i: inner diameter
- w: track width
- s: track spacing

for the WWCs:

- n: number of turns
- d: solenoid diameter
- d_0: wire diameter
- p: winding pitch

2.1.2 Self-inductance

Among the physical parameters that characterise a coil, one of the most important is the self-inductance (L) which is a measure of the induced magnetic field and, consequently, the induced voltage.

For a coil of a specified shape, the corresponding inductance, being related to the coil turns, the spacing of the turns, the inner and outer radii of the coil and the average diameter, can be

estimated knowing its geometrical properties. Therefore, the inductance formula given different shapes is:

$$L = \frac{\mu_0 N^2 d_{avg} c_1}{2} (\ln(c_2/\rho) + c_3\rho + c_4\rho^2) \quad (2.1)$$

where N is the number of turns, d_{avg} is the average diameter of the coil, μ_0 is the permeability in vacuum, C1−C4 are the parameters dependent on the coil shape, and ρ is the fill ratio of the coil, given by the following formula:

$$\rho = \frac{d_{out} - d_{in}}{d_{out} + d_{in}} \quad (2.2)$$

The d_{in} and d_{out} in Formula 2.2 are the inner and outer diameters of the coil, respectively.

In addition, the coil shape dependent parameters previously cited C_1−C_4 are in Table 2.1 below:

Coil Type	C_1	C_2	C_3	C_4
Quadrilateral	1.27	2.07	0.18	0.13
Hexagon	1.09	2.23	0	0.17
Octagon	1.07	2.29	0	0.19
Circle	1	2.46	0	0.2

Table 2.1: Inductance parameters for different shapes [32]

In electromagnetic terms, the self-inductance of a coil may be expressed as the measure of an inductor "resistance" to the change of the current flowing through the circuit and is also defined by dividing the total generated magnetic flux by the current present in the coil as follows:

$$L = \frac{N\Phi}{I} \quad (2.3)$$

where N is the coil's turns, I is the current in the coil, and φ is the magnetic flux crossing each turn of the coil.[33]

In an IPT system circuit, the coils also have terms of loss, as in Fig. 2.2.

2.1.3 Series parasitic resistance (R_{s1}, R_{s2})

This parasitic resistance is geometry, material and frequency dependent and its effect is given by 2 contributions: the physical effect of the skin and the current crowding effect.

- The skin effect is the tendency of an alternating electric current to exhibit maximum current density near the surface of the conductor, and decrease in depth, limiting itself to conduction near the surface. [34]

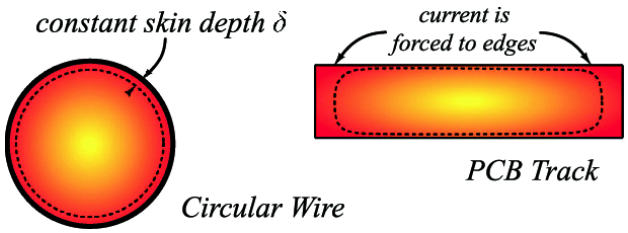

Figure 2.4: Skin effect [35]

In this situation, the effective cross-section area of the conductor through which the current flows is reduced. As a result, the effective resistance of the conductor increases slightly.

The formula that summarizes the parasitic resistance due to the skin effect is:

$$R_{skin} = R_{DC} \frac{t_0}{\delta\left(1-e^{-\frac{t_0}{\delta}}\right)} \frac{1}{1+\frac{t_0}{\omega}} \tag{2.4}$$

where R_{DC} is the resistance at zero frequency, the static resistance, equal to:

$$R_{DC} = \rho \frac{l_c}{A_c} \tag{2.5}$$

and ρ is the electrical resistivity of the material, $l_c = \pi \left(d - \frac{(\omega+s)n}{2}\right) n$ is the length of the conductive trace and A_c=ωt$_0$ is the cross-section area of the conductor with width w and thickness t$_0$.

Skin depth is

$$\delta(\omega) = \sqrt{\frac{2\rho_c}{\omega\mu}} \tag{2.6}$$

ρ_c being the conductivity and μ the permittivity of the metal trace.

- The current crowding effect is caused by eddy currents. Eddy currents are generated when the magnetic field of an external turn penetrates another metal trace perpendicularly to its surface. The magnitude of the eddy currents is proportional to the trace's resistivity and to the frequency of the magnetic field's changes.

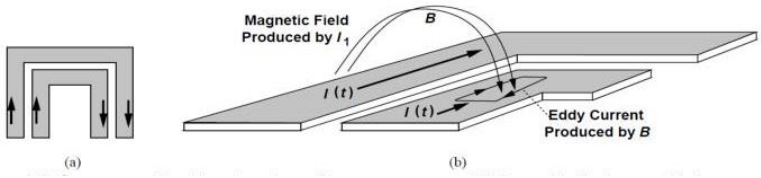

Figure 2.5:(a) Current distribution in adjacent turns (b) Detailed view of (a) and eddy current effect [36]

The parasitic resistance generate by the crowding effect is expressed as:

$$R_{eddy}(\omega) = \frac{1}{10} R_{DC} \left(\frac{\omega}{\omega_{crit}}\right)^2 \tag{2.7}$$

Therefore, the parasitic series resistance can be defined by Formula 2.8 as the sum of these two current effects:

$$R_s(\omega) = R_{skin}(\omega) + R_{eddy}(\omega) = R_{DC}\left(\frac{t_0}{\delta\left(1-e^{-\frac{t_0}{\delta}}\right)}\frac{1}{1+\frac{t_0}{\omega}} + \frac{1}{10}\left(\frac{\omega}{\omega_{crit}}\right)^2\right) \quad (2.8)$$

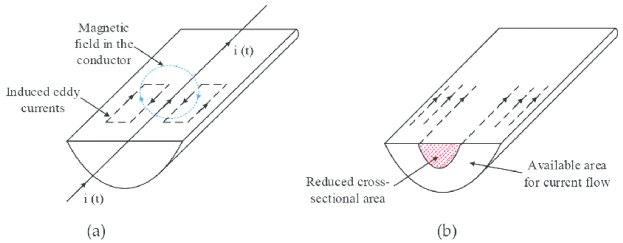

Figure 2.6: Total contributions (a)generated eddy currents and (b) skin effect [23]

2.1.4 Parallel parasitic resistance (R_{p1}, R_{p2})

Material dependent parameter and significant for low frequency and for materials with a small dielectric loss. In the case of IMDs, due to the high dielectric loss in the tissue, Rp is negligible for implanted coils, as for example in the case of the Rx [27].

$$\frac{1}{R_p(\omega)} = G_p(\omega) = \frac{\omega\varepsilon_0}{2}\left[\varepsilon_{r1}tan\delta_1\frac{K(k_1')}{K(k_1)} + (\varepsilon_{r2}tan\delta_2 - \varepsilon_{r1}tan\delta_1)\frac{K(k_2')}{K(k_2)} + \varepsilon_{r3}tan\delta_3\frac{K(k_3')}{K(k_3)} + (\varepsilon_{r4}tan\delta_4 - \varepsilon_{r3}tan\delta_3)\frac{K(k_4')}{K(k_4)} + (\varepsilon_{r5}tan\delta_5 - \varepsilon_{r4}tan\delta_4)\frac{K(k_5')}{K(k_5)}\right] \quad (2.9)$$

2.1.5 Parallel parasitic capacitance (C_{p1}, C_{p2})

The parallel capacitance depends on the thicknesses of the different materials in the spacing between conductive traces of the coil and the surrounding environment. When implanted, the high permittivity of tissue and fluids, increase significantly the parasitic capacitance of the coils, if compared to when they operate in air. In order to estimate the value of parasitic capacity, it is necessary to know the value of effective relative dielectric constant ε_{r-eff} of the structure taking in account the effect of all layers and their thickness. [37]

$$C_P = C_{ext} \cdot l_c + C_{OV} \tag{2.10}$$

where

$$C_{ext} = \varepsilon_{r-eff} C_0 = C_0 + C_{01} + C_{02} + C_{03} + C_{04} + C_{05} \tag{2.11}$$

C_0 is the capacitance between adjacent traces and C_{0i} $(i = 1{\sim}5)$ is the additional partial capacitance of each planar dielectric layer

$$C_0 = \varepsilon_0 \frac{K(k_0')}{K(k_0)} \ , \ k_0 = \frac{2s}{s+2\omega} \ , \ and \ k_0' = \sqrt{1 - k_0^2} \tag{2.12}$$

K(k_0) is the complete elliptic integral of the first kind.

ε_{r-eff} of coplanar PSC traces embedded multilayer structure can be found from

$$\varepsilon_{r-eff} = 1 + \frac{1}{2}(\varepsilon_{r1} - 1)\frac{K(k_0)K(k_1')}{K(k_0')K(k_1)} + \frac{1}{2}(\varepsilon_{r2} - \varepsilon_{r1})\frac{K(k_0)K(k_2')}{K(k_0')K(k_2)} + \frac{1}{2}(\varepsilon_{r3} - 1)\frac{K(k_0)K(k_3')}{K(k_0')K(k_3)} + \frac{1}{2}(\varepsilon_{r4} - \varepsilon_{r3})\frac{K(k_0)K(k_4')}{K(k_0')K(k_4)} + \frac{1}{2}(\varepsilon_{r5} - \varepsilon_{r4})\frac{K(k_0)K(k_5')}{K(k_0')K(k_5)} \tag{2.13}$$

$$k_i = \frac{\tanh\left(\frac{\pi s}{4t_i}\right)}{\tanh\left(\frac{\pi(s+2\omega)}{4t_i}\right)} \ , \ k_i' = \sqrt{1 - k_i^2} \tag{2.14}$$

where ε_{ri} and t_i are the relative dielectric constant and thickness of dielectric layers.

in Formula 2.10, l_c is the PSC conductor length, found from

$$l_c = 4 \cdot n \cdot d_0 - 4 \cdot n \cdot \omega - (2n+1)^2(s+\omega) \tag{2.15}$$

and the overlapping trace capacitance formula results

$$C_{OV} = \varepsilon_0 \varepsilon_{r\_eff\_ov} \frac{A_{ov}}{t_{ov}} \tag{2.16}$$

where A_{ov} is the overlapping area and t_{ov} is the spacing between the two metal layers, the effective dielectric constant between them can be found from

$$\varepsilon_{r\_eff\_ov} = \frac{\varepsilon_{r5}+1}{2} + \frac{\varepsilon_{r5}-1}{2}\left(1+\frac{12}{\frac{w}{t_5}}\right)^{-1/2} - \frac{\varepsilon_r - 1}{4.6}\frac{\frac{t_0}{t_5}}{\sqrt{\frac{w}{t_5}}} \tag{2.17}$$

Moreover, C_p has a main role in the resonance of the device as described in the next part. [37]

2.1.6 Matching capacitance (C_{s1}, C_2)

Capacitors C_{S1} and C_2 are inserted in the circuit in order to achieve the same oscillation frequency of the two coils (Tx and Rx) and maximize the matching in power terms. These capacitances are added to form a pair of resonant LC-tank circuits with L_1 and L_2, C_{s1}-Tx tank and Rx-C_2 tank respectively, in order to have the same resonance frequency in correspondence of the wanted operational frequency f_o. Resonance is achieved by having an LC tank circuit, a system composed of the coil as the inductor and a corresponding capacitor. The relationship between these components is defined as follows:

$$C = \frac{1}{L(2\pi f)^2} \tag{2.18}$$

where C is the capacitance of the resonant capacitor, L is the inductance of the coil, and f is the operating frequency.[38]

In order to enhance efficiency in the transmission of power of the inductive transmission system, the transmitter and receiver are tuned with the same resonant frequency f_0

$$f_0 = \frac{1}{2\pi\sqrt{LC}} \tag{2.19}$$

Different types of LC tank circuits are used for different purposes, but usually an IPT system that operates in the near field has a transmitter system with a series LC tank, and a receiver system with a parallel LC tank. The efficiency of power transfer (PTE) is greatly affected by the proper tuning of the LC tank. [39]

Moreover, it is important to underline that the tanks' resonating frequency is and must be different from the SRFs of the single coils.

2.2 Inductive parameters

2.2.1 Self-resonance frequency

For an ideal coil, without the loss terms, the impedance will result as Z = sL = j2πfL and the relation between the impedance and the used frequency would be linear as shown in Fig. 2.7.

When in a WPT circuit, the coil would be affected to parallel capacitance Cp, as reported above, that will actually modify the impedance of the real coil to

$$Z = \frac{sL}{s^2 LC_p + 1} \tag{2.20}$$

with s=j2πf

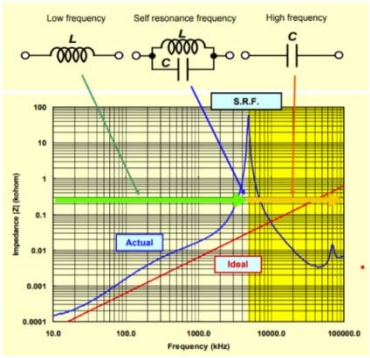

Figure 2.7: Impedance of an ideal (red) and real (blue) coil. [1]

In this real case, the magnitude of the impedance in the bode diagram will assume a spike, the presence of a double pole, in correspondence with a frequency known as self-resonance frequency of the coil (f_{SRF}) and equal to

$$f_{SRF} = \frac{1}{2\pi\sqrt{LC_p}} \tag{2.21}$$

At the f_{SRF} level, the inductor and capacity Cp resonate resulting in a high impedance. Due to the existence of the parasitic capacitor, when a high frequency current is used, most current in the coil would be bypassed via the parasitic capacitor. As a result, the coil cannot be viewed as an inductor anymore. [25]

This frequency cuts the behavior of the coil which for frequencies lower than the f_{SFR} behaves like an inductor and for frequencies higher than f_{SFR} its behavior is regulated by the capacitance. Roughly speaking, the effect of C_p can be neglected for a frequency $f_o \leq f_{SRF}/10$. Therefore, it is usually a adequate idea to choose an operating frequency under the f_{SRF}. [1]

2.2.2 Quality factor

As all the loss elements as been presented, the equivalent impedance of all the lumped circuit it is summarized as:

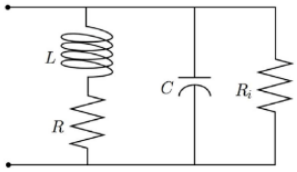

Figure 2.8: Electromagnetic coil equivalent circuit model [40]

$$Z(\omega) = \frac{R_s + j\omega L}{(R_s + j\omega L)(G_p + j\omega C) + 1} \tag{2.22}$$

where R, L and C is the coil resistance, inductance, and parasitic capacitance respectively.

This impedance can be given as a sum of a real and an imaginary component. These two components represent for the real component all energy loss in the coil, while the imaginary component represents all energy storage in the coil. [25]

Through this value it is possible to calculate one of the most significant electromagnetic parameters: the Quality factor. The Quality factor or Q factor is a dimensionless parameter that quantify the coil capacity to generate high or low magnetic field, that represents the ability to transfer power.

Q factor can be expressed from the equivalent impedance Z of the lumped circuit of Fig. 2.2 as the ratio of the imaginary part over the real part:

$$Q = \frac{Im(Z)}{Re(Z)} \tag{2.23}$$

High Q indicates a low rate of energy loss relative to its stored energy in the power antenna. Q factor decreases to zero at the SRF and accordingly, designed coils are usually supposed to guarantee a valuable work at a frequency in which there is the maximum Q factor.

As mentioned, Rp is negligible for implanted coils thus the formula for the quality factor is simplified into

$$Q(\omega) = \frac{\omega L - \omega C_p \left(R_s^2 + \omega_p^2 L^2\right)}{Rs} \tag{2.24}$$

Higher its value, better its power transfer behaviour since, as explained, the Q indicates energy loss relative to the amount of energy stored within the system.

2.2.3 Mutual inductance

Mutual inductance occurs when a change in current in a coil induce an EMF in a second coil place near the first one. When the magnetic field of a coil crosses another near coil, the mutual inductances generate is equal to:

$$\begin{cases} M_{21} = \frac{N_2 \Phi_{21}}{I_1} \\ M_{12} = \frac{N_1 \Phi_{12}}{I_2} \end{cases} \tag{2.25}$$

where φ_{21} is the magnetic flux generated by the first coil and intercepting the second coil, and φ_{12} the magnetic flux generated by the second coil and intercepting the first coil. The following equation can be state:

$$M = M_{21} = M_{12} \tag{2.26}$$

Since mutual inductance is related to the coil geometry and distance between the coils, is also possible to express it as:

$$M_{12} = \theta \sum_{i=1}^{N_1} \sum_{j=1}^{N_2} M(x_i, y_j, d_{12}) \tag{2.27}$$

$$M(x, y, d_{12}) = \mu_0 \sqrt{xy} \left[\left(\frac{2}{\gamma} - \gamma \right) K(\gamma) - \frac{2}{\gamma} E(\gamma) \right] \tag{2.28}$$

$$\gamma = \sqrt{\frac{4xy}{(x+y)^2 + d_{12}^2}} \tag{2.29}$$

using complete elliptic integrals K(k) and E(k), the spatial coordinates (x, y) and d_{12} the distance between the coils.

In order to define the degree to which the mutual inductance reaches maximum, we refer to the term coupling coefficient k. It can be defined by the self and the mutual inductances as follow:

$$k = \frac{M}{\sqrt{L_1 L_2}} \tag{2.30}$$

or

$$M = k\sqrt{L_1 L_2} \tag{2.31}$$

It describes the coupling between the two coils, and it ranges from a minimum of 0, indicating no inductive coupling, to a maximum of 1, indicating a full or maximum inductive coupling. [37] [23]

2.2.4 Power transfer efficiency and power delivered to the load

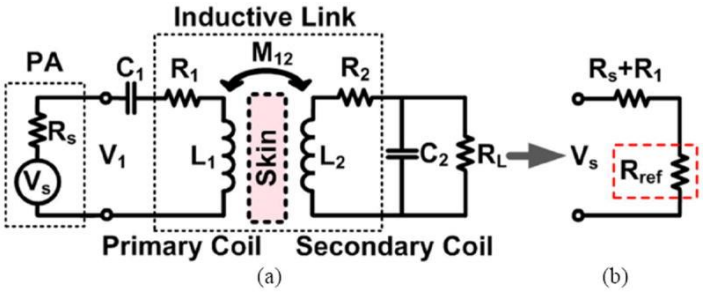

Figure 2.9: (a) Lumped circuit model of the inductive power transmission (b) Equivalent circuit at resonance [38]

two important parameters in IPT systems are the Power Transfer Efficiency (PTE) and the Power Delivered to the Load (PDL).

As seen in the previous section, tuning the LC tanks at the same resonance frequency, f_0, allows to achieve the highest PTE and PDL.

$$f_0 = 1/2\pi\sqrt{L_1C_1} = 1/2\pi\sqrt{L_2C_2} \tag{2.32}$$

Fig. 2.9 shows this case of resonance, in which the effect of the secondary side on the primary side of the circuit can be modelled as an impedance expressed as

$$R_{ref} = k_{12}^2\omega_0 L_1 Q_{2L} \tag{2.33}$$

where k_{12} is the coupling coefficient between L_1 and L_2, and $Q_{2L} = Q_2Q_L / (Q_2+Q_L)$, in which $Q_2 = \omega_0 L_2 / R_2$ and $Q_L = R_L / \omega_0 L_2$, often referred to as the load quality factor.

At resonance, the equation for PTE, η, considers the power provided by the source power (V_s) divided between the impedances $R_s + R_1$ and R_{ref} and the power from R_{ref}, received by the secondary loop, is divided between R_2 and R_L . This leads to an expression of power division between the existence resistances

$$\eta = \frac{R_{ref}}{R_s+R_1+R_{ref}} \cdot \frac{Q_{2L}}{Q_L} = \frac{k_{12}^2 Q_1 Q_{2L}}{1+k_{12}^2 Q_1 Q_{2L}} \cdot \frac{Q_{2L}}{Q_L} \tag{2.34}$$

where $Q_1 = \omega_0 L_1 / (R_s + R_1)$ is the quality factor of the Tx.

From this equation it can be seen that, in order to achieve the highest PTE, R_{ref} should be maximised.

Concerning the Power delivered to the load (PDL), it can be calculated by multiplying the power provided by V_s, $V^2_s/2(Rs+R1+Rref)$, with the PTE from (2.34), obtaining

$$P_L = \frac{V_s^2 R_{ref}}{2(R_s+R_1+R_{ref})^2} \cdot \frac{Q_{2L}}{Q_L} = \frac{V_s^2}{2(R_s+R_1)} \frac{k_{12}^2 Q_1 Q_{2L}}{(1+k_{12}^2 Q_1 Q_{2L})^2} \cdot \frac{Q_{2L}}{Q_L} \tag{2.35}$$

A two-port IPT system may be modelled, as well as its terms, using impedance parameters. Fig. 2.10 illustrates this kind of generic model

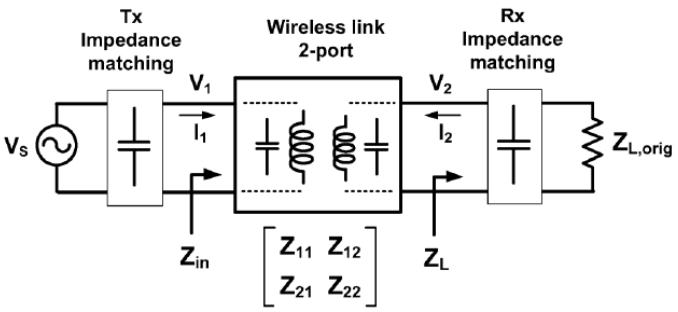

Figure 2.10: Model of two-port wireless power transmission using impedance (Z) parameters. [43]

Using impedance parameters is possible to express the two power terms exploited, PTE and PDL.

For PTE

$$PTE = \frac{Re(Z_L)}{Re(Z_{in})} \frac{|Z_{21}|^2}{|Z_{22}+Z_L|^2} \tag{2.36}$$

where $Z_{in} = Z_{11} - Z_{12}Z_{21}/(Z_{22} + Z_L)$.

If the implant size and the coupling between the external Tx and implanted Rx is very small, then the PTE can be approximated as

$$PTE \approx \frac{|Z_{21}|^2}{Re\,(Z_{11})|Z_{22}+Z_L|} \frac{Re\,(Z_L)}{|Z_{22}+Z_L|} \tag{2.37}$$

Under resonance, denoting R_{11}, R_{22}, and R_L as the real parts of Z_{11}, Z_{22}, and Z_L, respectively, we can further simplify (2.37) to

$$PTE \approx \frac{|Z_{21}|^2}{Re_{11}(R_{22}+R_L)} \frac{R_L}{(R_{22}+R_L)} = \frac{|Z_{21}|^2}{|Im\,(Z_{11})\,Im(Z_{22})|} \frac{|Im(Z_{11})|}{R_{11}} \frac{|Im(z_{22})|}{(R_{22}+R_L)} \frac{R_L}{(R_{22}+R_L)} = k^2 Q_{TX} Q_L \eta_{RX} \tag{2.38}$$

Where k is the coils' coupling coefficient including both the real and imaginary part, and Q_{TX} is the Q-factor of the Tx. This expression motivates the definition of another parameter, the Tx-FoM, which indicates how strongly the transmitter is coupled with the receiver

$$Tx - FoM = k^2 Q_{TX} \tag{2.39}$$

It is also present in the expression the term Q_L, the loaded Q of Rx, and the last term in (2.38) is the Rx internal efficiency expressed as

$$\eta_{RX} = \frac{R_L}{(R_{22}+R_L)} \tag{2.40}$$

which shows what portion of the received power is delivered to the load, R_L, and what portion is dissipated in R_{22}.

Also, the PDL can be expressed in impedance terms. The PDL at resonance can be written as:

$$PDL = |I_2|^2 R_L = |I_1|^2 \frac{|Z_{21}|^2}{|Im(Z_{11})Im(Z_{22})|} \times |Im(Z_{11})| \frac{|Im(Z_{22})|}{R_{22}+R_L} \frac{R_L}{R_{22}+R_L} \tag{2.41}$$

$$PDL = |I_1|^2 k^2 |Im(Z_{11})| Q_L \eta_{RX} = |I_1|^2 k^2 |Im(Z_{11})| R_x - PRS \tag{2.42}$$

Where I_1 and I_2 are currents flowing into ports 1 and 2 in Fig. 1, respectively. It can be seen that Q_L and η_{RX} represent the properties of Rx only, and so they can be replaced with the Rx-PRS defined as

$$R_x - PRS = Q_L \eta_{RX} \tag{2.43}$$

and indicates how strongly the Rx can receive power under a given magnetic field.

In conclusion to give a synthetic expression of PTE dependent on the illustrated parameters, it is easy to individuate the expression

$$PTE = T_x - FoM \times R_x - PRS \tag{2.44}$$

[42]

2.3 Safety limits

Tissue energy absorption is also a significant term in IPT systems. This depends on the tissue type and on the electric field (E) generated which is related to the power transmitted and the frequency of transmission. One definition of the Specific Absorption Rate (SAR) is:

$$SAR = \frac{\sigma |E_{rms}|^2}{\rho} \tag{2.45}$$

where: σ is the tissue's electrical conductivity, ρ is its density; and is E_{rms} the induced electric field's round value.

In this regard, the maximum average Specific Adsorption Rate (SAR) for the human skull, according to the Federal Communications Commission (FCC), is 1.6 W/Kg for 1g of tissue mass recorded over a period of 6 minutes [44].

The electric field E in Formula 2.45 can be retrieved because the coil inductors are magnetically connected through a magnetic field B. According to Maxwell's equation

$$\nabla \times E = -\frac{\partial B}{\partial t} \propto \omega_p I_1 \tag{2.46}$$

where I_1 is the alternated current that flows in L_1 with an angular operating frequency of $\omega_p = 2\pi f_o$. It is clear from the Formula 2.46 that

$$SAR \propto (f_0 \times I_1)^2 \tag{2.47}$$

This relation is intriguing since it affirms that by appropriately lowering the operating frequency, the primary coil's current flow can be increased while maintaining a constant SAR. If the PTE stays high for low operating frequencies, the PDL can be increased without going above the SAR limit. [38]

Concerning the value of frequency used, the RF in the near-field area is used by the majority of medical applications that use IPT (from kHz to few GHz). Anyway, the use of this band is

highly controlled for safety reasons since, as seen, all devices have to respect requirements about heat absorption.

Available ISM bands
6.765 MHz - 6.795 MHz
13.553 MHz - 13.567 MHz
26.957 MHz - 27.283 MHz
40.66 MHz - 40.70 MHz
83.996 MHz - 84.004 MHz
167.992 MHz - 168.008 MHz
433.05 MHz - 434.79 MHz
886 MHz - 906 MHz
2.4 GHz - 2.5 GHz
5.725 GHz - 5.875 GHz
24.0 GHz - 25.25 GHz
61.0 GHz - 61.5 GHz
122 GHz - 123 GHz
244 GHz - 246 GHz

Table 2.2:List of ISM bands [45]

The user must choose between ranges that are designated for Industrial, Scientific, and Medical applications, often known as ISM bands, to determine the frequency at which IPT operates, or f_o. The (ITU) has defined these bands for non-telecommuting uses (Table 2.2).

2.4 Optimization algorithms for inductive coupling

Due to many parameters influencing the power transfer efficiency and the ability of one parameter to affect others, computing the specific parameters variable is very challenging and time-consuming. In order to develop an IPT system which satisfies the IMD requirements, several parameters have to be settled and chosen.

To overcome this problem and need, researchers relied on simulation systems capable of testing different geometries and system designs. In addition, alongside the simulation systems, strategies have been developed based on optimization algorithms able to test and relate the different system parameters and identify the set of parameters that allows to obtain the most performing design.

Many optimization algorithms used, aiming at maximising system efficiency, are based on different types of artificial neural network (ANN) [46], as genetic algorithm (GA)[47] or on a simple flowchart that suggests step by step the procedure as the case of [48] and [43].

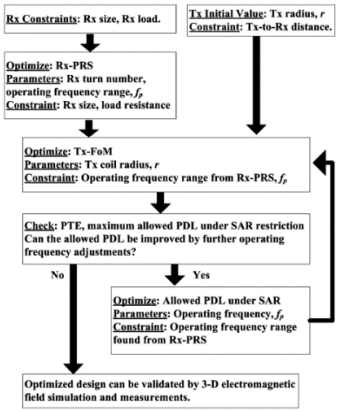

Figure 2.11: Example flowchart of an optimization algorithm [43]

In conclusion, these algorithms were introduced in order to find the variable and better correlation between the parameters, but it is reasonably crucial taking account of the constraints of the system and developing suitable equations related to parameters to produce suitable and reliable results.

3. Design simulations

As seen in the previous paragraph, IPT systems are widely used in the biomedical field and can really be a valid possibility regarding wireless power transfer in NIs.
When inserted within an IMD, the power delivery system must comply with the minimum requirements, the criteria in terms of safety and exchanged power allowing the correct operation of the device. In order to do this, simulation systems are used to optimise the design and efficiency of the tested IPT device and its parameters.

3.1 Materials and methods

In order to carry on the simulations of the IPT system, the focus was on what concerns the coupling elements of the system: the transmitter and receiver coils.

All simulations were conducted using the Ansys HFFS software through which it is possible to simulate more or less complex systems that are designed to work in high frequency conditions and with application of different types of fields.

Initial simulations focused on the implantable part of the device, the receiver, studying the characteristics and performances first in the air and then taking into account the effect of the surrounding tissues.

Proceeding with the subsequent simulations, the coupling between the transmitter and receiver was considered and studied, again, first evaluated in air and then, simulating the complete system, in the presence of the tissues.

.

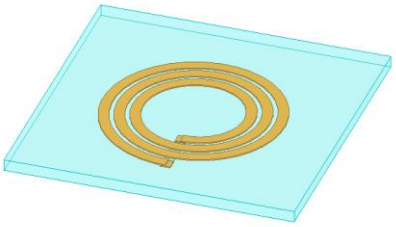

Figure 3.1:Receiver model

Regarding the Rx, it was simulated considering the constraints applied by the implant location, inside the blood vessel. The receiver is therefore developed as a PSC coil type made with bioresorbable material, in our case magnesium, of thickness equal to 20 μm, with an outer diameter of 3.36 mm [1] and totally encapsulated in a PCL layer of 200 μm of thickness and dimensions 5x5 mm. To realize the desired spiral shape in this simulation, on Ansys the use of the function "PoligonHelix1" was exploited and the materials for the encapsulation layer (PCL) and the coil have been characterized with relative permittivity and conductivity.

Moreover, the system has been studied with the imposition of a lumped port excitation (R_{in}= 50 Ω) applied to the two ends of the coil to evaluate the scattering parameters of the simulated design. The impedance value R_L was subsequently modified and assessed for different values.

Concerning the simulations in air, coil and PCL encapsulation layer are placed at the center of the simulation environment, consisting of a cubic box of air (500 mm side), to which the radiation boundary condition is applied and frequencies from 10 MHz to 5 GHz are evaluated.

The main parameters which were evaluated during the simulations on the receiver were the Q factor which, as we have seen, is an index of good electromagnetic properties and performance of the coil and the parameter of L inductance, studying its behaviour while changing several coil's parameters.

Regarding the geometric parameters evaluated, the number of turns, width and space gap of the Rx coil were varied respectively in the ranges of values reported in table 3.1.

Coil parameter	[initial value:step:final value]
n_2: number of turns (Rx)	[2:1:5]
w_2: width trace (Rx)	[0.08:0.02:0.2] mm
s_2: space gap (Rx)	[0.08:0.02:0.18] mm

Table 3.1: Rx sweep parameters in air simulation

Moving on, simulations in the presence of tissues were conducted. In order to evaluate parameters in this situation, the Q factor and L inductance for the Rx inserted into tissues were evaluated and the variations with respect to the in-air environment were observed.

Keeping the elements of the simulation (coil and encapsulation layer) identical to the previous one in air, the environment set up in which the receiver was immersed has been modified. In fact, the several layers of tissue were simulated as layers of length and width equal to 80x80mm and each with the respective average thicknesses from the literature, reported in the table 3.2.

skin	2mm
fat	2 mm
muscle	4 mm
skull	10 mm
dura	1 mm
CSF	2 mm
endothelium	0,0005 mm
blood	3,5 mm
grey matter	50 mm

Table 3.2: tissues layer thickness

In in vivo-like conditions the receiver is placed inside the blood vessel (in SSS) and, therefore, during simulation in tissues, the receiver coil is located inside the blood layer (Fig 3.2).

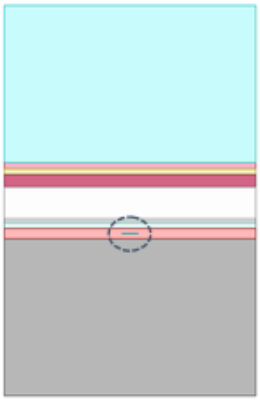

Figure 3.2: Rx in tissues simulation model

Moreover, each tissue has been characterized with its own values of relative permittivity and conductivity, variable to the frequencies of interest. Moreover, in simulation with tissues the radiation boundary condition is applied all around the box made up of tissues and air box.

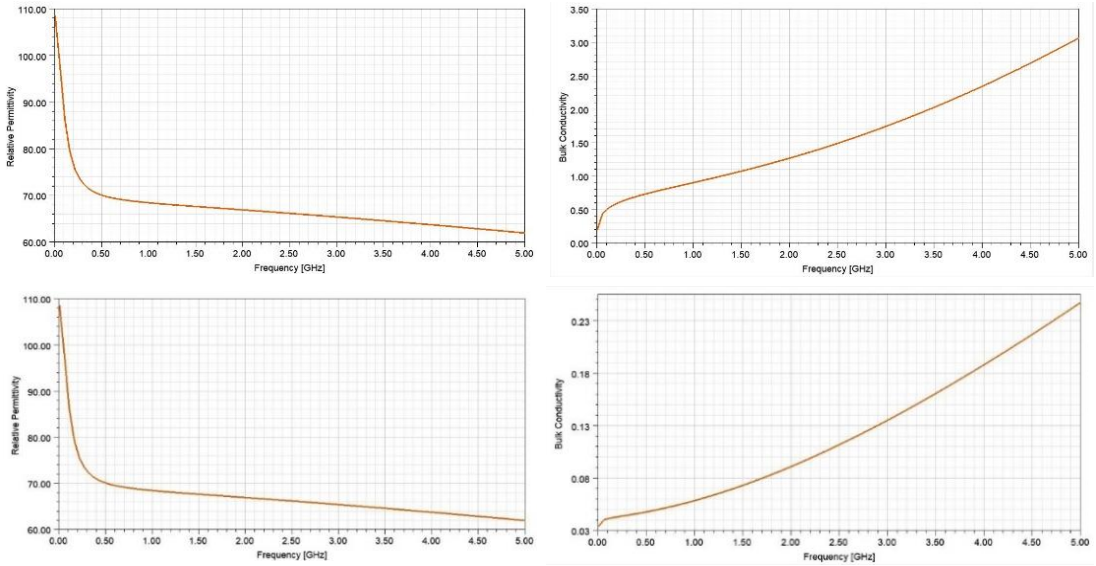

Figure 3.3:Example of permittivity and conductivity characterization of tissues

After studying the characteristics of the single Rx coil, the coupling between Tx and Rx was subsequently studied and simulated by testing the two coils first in the air, and then in implanted conditions.

In order to simulate the coupling between the two coils, the receiver was modelled in the same way as in the previous simulations, encapsulated in the PCL layer. For the transmitter, the 'RectHelix1' function was used to model the copper spiral with a height of 36.5 µm and placed

on a 1.55 mm thick, 50x50 mm layer of FR4 to simulate a printed circuit board. Moreover, a lumped port excitation (R=50 Ω) with an output power of 1 W was inserted at the coil extremities of the transmitter.

In the air simulation environment, the receiver is placed at the centre of the air box (100 mm side) and the transmitter 23.75 mm away from the receiver and facing towards it (FR4 layer above).

Frequencies from 10 MHz to 5 GHz were evaluated.

The sweep parameters in this case, additionally to the receiver properties already explored, were also the geometrical parameters of the transmitter, allowing the evaluation of different designs. All the variations studied in this type of simulation for Rx and Tx are specified in the table:

Coil parameter	[initial value: step: final value]
n_1: number of turns (Tx)	[1:1:7] turns
w_1: width trace (Tx)	[0.5:0.25:2.25] mm
s_1: space gap (Tx)	[0.25:0.25:1.75] mm
D_{o1}: outer diameter (Tx)	[16:2:30] mm
n_2: number of turns (Rx)	[2:1:5] turns
w_2: width trace (Rx)	[0.08:0.02:0.2] mm
s_2: space gap (Rx)	[0.08:0.02:0.18] mm

Table 3.3:Rx and Tx sweep parameters in air simulations

Focusing on the electromagnetic characteristics of the transmitter, the Q factor of the transmitter was evaluated as certain geometrical parameters changed. In this type of simulation, moreover, based on the coupling of the two coils, the inductive parameters to be observed were also the PTE and PDL, attempting to study how the geometrical parameters influenced their value.

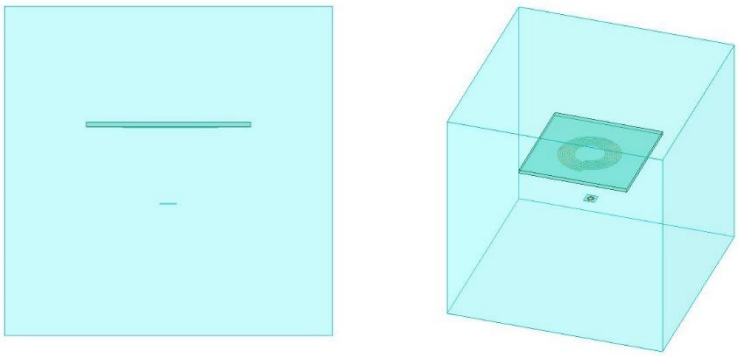

Figure 3.4: Tx and Rx in air simulation model

Finally, as the ultimate goal of the simulations, a further model was developed which aims to become a complete model for studying the inductive link between receiver and transmitter in an IPT system to be integrated with a neural interface.

The complete simulation model thus includes:

- Receiver
- Transmitter
- Tissues

The structure of the receiver and transmitter coils used is the same as described in the previous section, as is the structure of the interposed tissues and their characterisation by the most relevant conductive properties.

The transmitter is placed facing the receiver above the skin layer and inserted into the air layer.

The aim of this last set up of simulations is to test the system in its entirety and arrive at a design for the two coils that guarantees the optimisation of the system in terms of power.

As seen in a previous part (paragraph 2.4), optimisation algorithms are often used to obtain the design that achieves the best performance.

An optimisation algorithm developed in a previous work [48]was therefore used, which is based on performing simulation steps on the different elements of the simulated system and results in the optimisation of the entire system.

In Fig. 3.5 the flowchart of the algorithm used is shown:

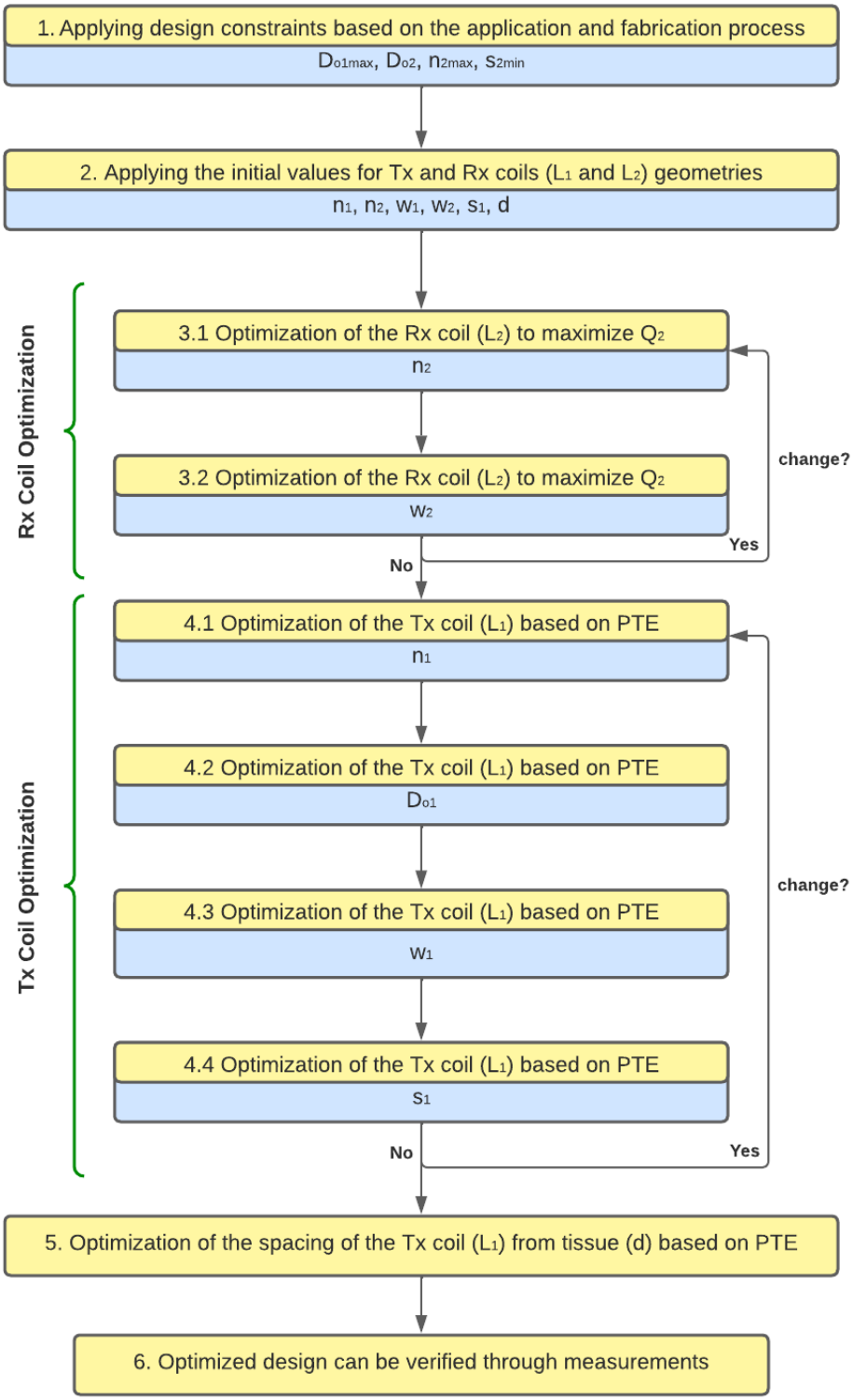

Figure 3.5: Algorithm flowchart

Examining each of the steps, it becomes clearer as this algorithm aims to optimise the system by optimising each individual element.

1. In the first step, the constraints given by the application and manufacturing process are assessed.

   In the case of this project, the major constraints concern the receiver, due to its location in the implant and the microfabrication required for its manufacture.

   In particular,

   - Outer diameter (D_{o2}): the diameter of the coil is limited to 3.36 mm in order to comply with implantation limits.
   - Number of turns (n_{2max}): maximum number of turns of the receiving coil set at 5, as difficulties were encountered during manufacture for a higher number of turns. [1]
   - Space gap (s_{2min}): for spacings smaller than 0.08 mm, the handling of turns during manufacture is made more complicated[1].

   and the relative constraints on the other parameters reasonably to the geometric limits imposed by the above mentioned.

   As far as the Tx is concerned, the only purpose posed was to ensure that it was as portable as possible, imagining future application, and, therefore, it was decided to test an

   - outer diameter (D_{o1max}): maximum for the Tx coil equal to 30 mm

2. In the second step, the geometric values of Tx and Rx are initialised to establish a starting design:

INITIAL VALUES	
Parameter	Value
n_1: number of turns (Tx)	3 turns
w_1: width trace (Tx)	1 mm
s_1: space gap (Tx)	0.5 mm
D_{o1}: outer diameter (Tx)	22 mm
n_2: number of turns (Rx)	4 turns
w_2: width trace (Rx)	0.16 mm
s_2: space gap (Rx)	0.08 mm
Distance Tx-skin	1 mm

Table 3.4: Parameters' initial values

3. The third step, divided into 2 sub-steps, is focused on the optimisation of the receiver according to the Q factor value of the coil obtained in the variations of the geometrical parameters of the coil.

   3.1) Starting from the initial values of the simulation, the algorithm suggests varying the number of turns of the Rx (n_2) while keeping the spacing value between the turns equal to the s_{min}, which in the current case is equal to 0.08 mm, since lower values of s_2 result in higher values of Q factor.
   This step leads to selecting a value of n_2 for which the Q factor is higher.

   3.2) Using this value for n_2, proceed to the next step by testing different values of width trace (w_2) and again select the value of w_2 for which the Q factor is highest.

Coil parameter	[initial value: step: final value]
n_2: number of turns (Rx)	[2:1:5] turns
w_2: width trace (Rx)	[0.08:0.02:0.2] mm

Table 3.5: Step 3 algorithm - Rx sweep parameters

Steps 3.1 and 3.2 were repeated until there was no change in them.

4. The fourth step is subdivided into four sub-steps, each of which is dedicated to testing the different parameters of the Tx.
   In the case of the transmitter, each parameter was selected by evaluating the PTE value obtained and selecting the value that would maximise the PTE for each geometric parameter tested. In order, first n_1, then D_{o1}, w_1 and finally s_1 were varied.

   Again, the steps were then repeated until they were no longer varied, and the selection was then made to obtain higher PTE values.

   The variations evaluated were therefore:

Coil parameter	[initial value: step: final value]
n_1: number of turns (Tx)	[1:1:7] turns
D_{o1}: outer diameter (Tx)	[16:2:30] mm
w_1: width trace (Tx)	[0.5:0.25:2.25] mm
s_1: space gap (Tx)	[0.25:0.25:1.75] mm

Table 3.6: Step 4 algorithm – Tx sweep parameters

4. Finally, step 5 aims to find the right distance between Tx and skin layer to maximise the PTE.
   The distances tested were:

Parameter	[initial value: step: final value]
Distance spacing skin-Tx	[1 :0.25 :3] mm

Table 3.7: Step 5 algorithm – Tx-skin distance sweep

Fig. 3.6 shows the simulation set-up of the complete system:

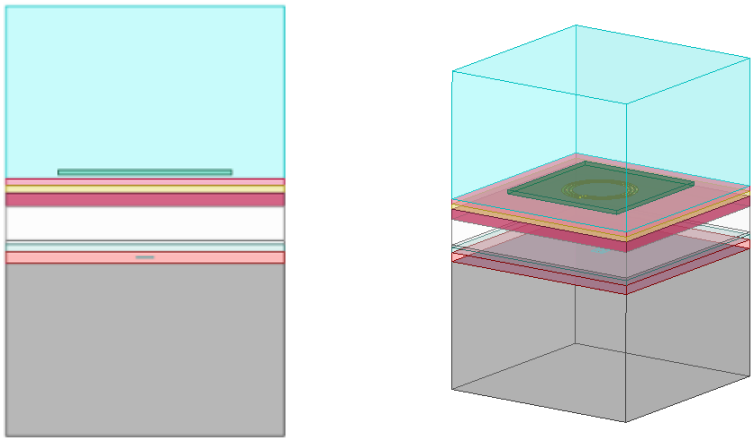

Figure 3.6: Tx and Rx in tissues simulation – complete system

In addition to the system properties observed at each step to select the value of the parameter under consideration, the parameters observed in this final simulation concern the system's power transfer terms and thus PTE and PDL, but the SAR value produced by the system was also evaluated at the end of the optimisation steps.

The previous simulations refer to the complete system of coil transmitter and coil receiver during the implantation. In this case, the receiver fabrication method based on laser cutting of a 20µm-thick magnesium foil was considered.[1]

It was subsequently decided to manufacture the receiver using an alternative method based on the evaporation of magnesium and no longer by laser cutting. Through measurements, the thickness of magnesium deposited during the selected evaporation time varied between 1 and 2 µm. It was therefore decided to conduct further simulations using the optimised design obtained through the simulation of the entire system in the tissues with a variation in the receiver thickness, which was simulated for the following values

Parameter	[initial value: step: final value]
Rx thickness	[1 :0.5 :2] µm

Table 3.8: Rx thickness sweep

The primary aim of these simulations was to investigate the feasibility of gathering and transporting power wirelessly with these reduced thicknesses.

3.2 RX results

The study of Rx allows one to better understand the electromagnetic properties of the proposed coil and to study how they vary as the simulation environment changes.

3.2.1 Rx results - in air simulation

The values of the Rx parameters (Q factor and inductance) calculated in air, being not attenuated by any tissues, appear rather high considering the small size of the coil and especially the material of which it is composed (section 1.4.1.1) not generally employed.

As far as the calculated Q factor is concerned, the values taken by varying the geometrical parameters of the receiver were compared. The graphs below show the results.

It was found that in air:

- For smaller w_2 measurements (w_2= 0.08, 0.1, 0.12 mm), as the number of coil turns increases, the Q factor increases (Fig. 3.7)

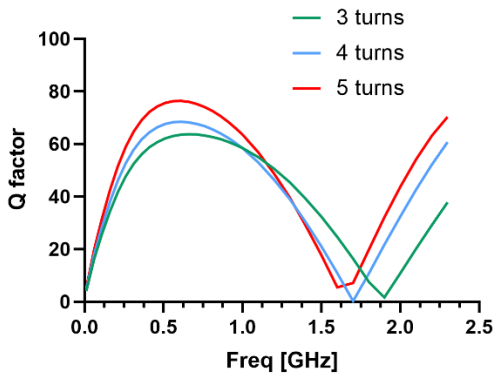

Figure 3.7: Rx Q factor varying Rx turns (w_2=0.1mm, s_2=0.1mm)

- For larger w_2 measurements (w_2=0.14, 0.16, 0.18 mm), as the number of turns increases, the Q factor value decreases.

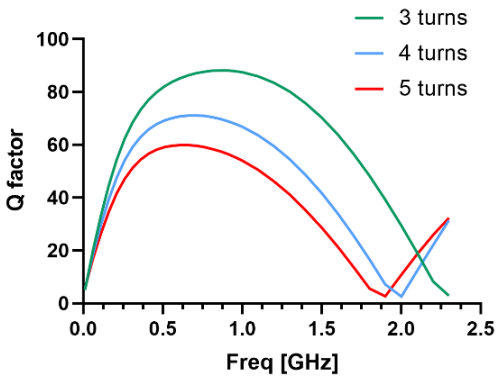

Figure 3.8: Rx Q factor varying turns (w_2=0.14mm, s_2=0.1mm)

Considering the SRF, visible through the graphs of the Q factor at the point where the parameter goes to zero, it can be seen that as the number of turns increases, the SFR decreases. The variation of the width doesn't seem to affect the trend, for small values of width. However, when the width is larger than XX, an increase in the SRF is noticeable.

Analysing the Q factor when varying another geometric parameter of the receiver, the spacing value between turns, we obtain that the maximum values of the Q factor are observed for lower values of space gap (Fig. 3.9).

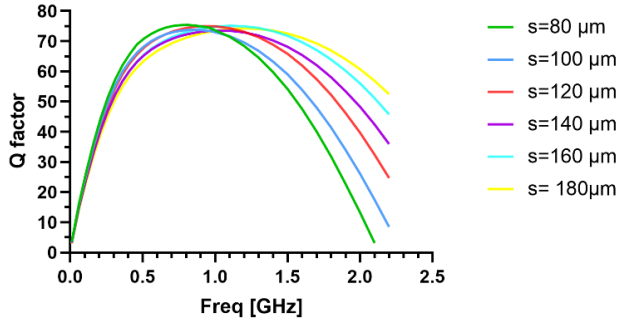

Figure 3.9: Rx Q factor varying space gap (n_2=3, w_2=0.1mm)

Moving on to analyse the other fundamental parameter for the electromagnetic characteristics of the coil, inductance was evaluated as the number of turns of the receiver varied.

In Fig. 3.10 it can be seen that as the number of turns tested increases, the inductance increases, assuming an almost linear behaviour.

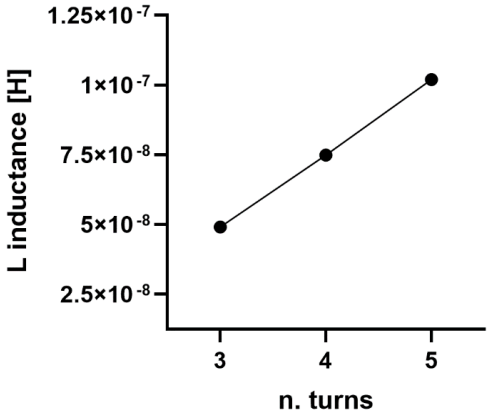

Figure 3.10: Rx inductance varying turns (w_2=0.08mm, s_2=0.1mm)

Finally, when evaluating the variation of inductance with respect to trace width, it assumes lower values for higher width values.

The results obtained are in line with what was expected when evaluating the inductance equation (Formula 2.1). The parameter is found to be directly proportional to the number of turns and the d_{avg} of the coil, which, in the case of the coil with the larger width trace, tends to assume lower values for an equal number of turns.

It is important to specify that it is desirable to use designs in which the inductance value is high, as this allows not only good magnetic coupling, but also the use of a smaller matching capacitance in the design.

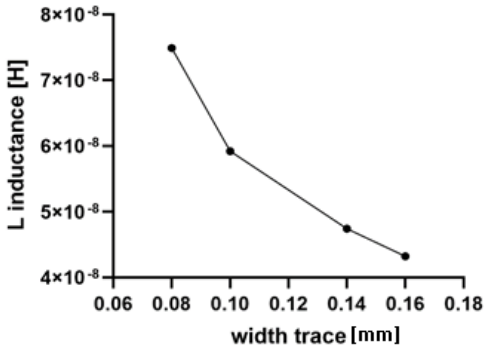

Figure 3.11: Rx inductance varying width trace (n_2=4 turns, s_2=0.1mm)

3.2.2 Rx results - in tissues simulation

The results regarding the simulations of the receiver inside tissues led to expected results, the Q factor parameter and the inductance in fact turned out to be lower than the values obtained from the simulation in air. This was to be expected since, in this case, the presence of the tissues with their properties and characteristics attenuates the coil's magnetic characteristics and performances.

Evaluating the results for the Q factor of the receiver as the number of turns varies, increasing the number of turns of the receiver, led to an increasing value of the Q factor.

This trend is similar to that obtained when simulating in the absence of tissues, but with lower values: while in air the results reached values up to 80, in the presence of the tissues for the same number of turns, width and space gap, the results are below 60, as can be seen in Fig. 3.12

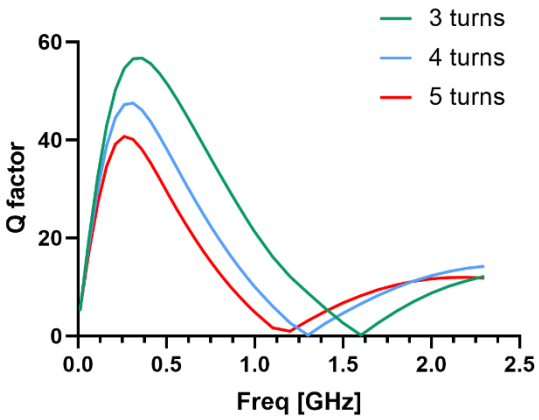

Figure 3.12: Rx Q factor varying turns (w_2=0.16mm, s_2=0.08mm)

Comparing the value of the Q factor when varying the coil width, as the width increases, the Q factor increases, and again a lowering of the value of the parameter due to the attenuation by the tissues can be observed

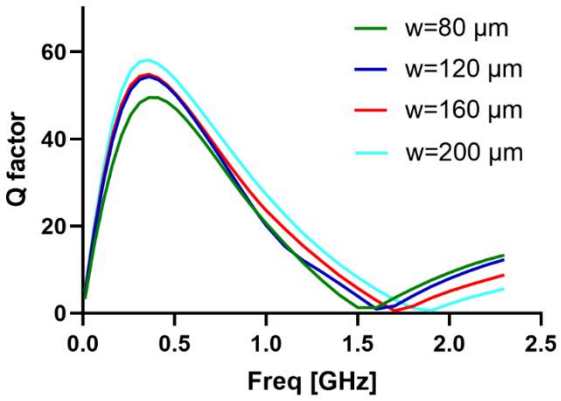

Figure 3.13: Rx Q factor varying width trace (n_2=3 turns, s_2=0.12mm)

As far as the inductance value is concerned, again the trend remains the same as in the case of the simulation in air, and thus as the width of the coil increases, a decrease in the inductance value is observed.

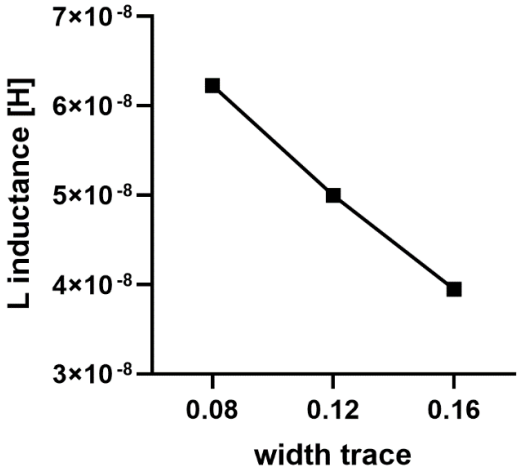

Figure 3.14: Rx inductance varying width trace (n_2=4 turns, s_2=0.08mm)

On the other hand, evaluating the behaviour of the inductance, as the number of turns increases, its value increases, reaching tenths of nH.

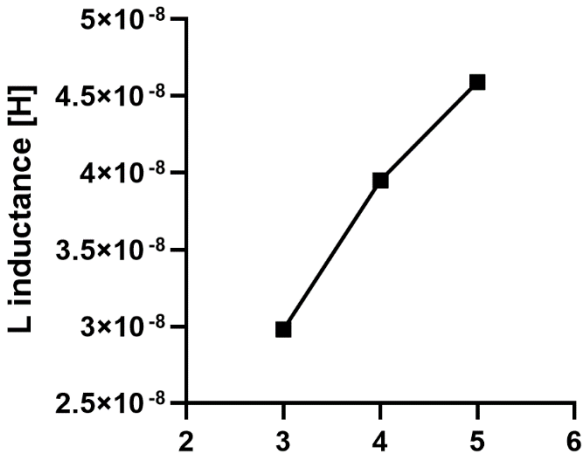

Figure 3.15: Rx inductance varying turns (w_2=0.16mm, s_2=0.08mm)

3.3 Tx and Rx results

Evaluating the system containing both transmitter and receiver, the coupling behaviour between the two coils is observed.

3.3.1 Tx and Rx results - in air

Studying the system of Tx and Rx together and having already discussed the characteristics of the receiver in the previous paragraphs, it is interesting to evaluate the electromagnetic characteristics of the Tx inserted in this system.

The behaviour of the Tx with regard to its Q factor is not as predictable and linear as that of the receiver. It can be seen that from low values of turns to higher values, the Q factor tends to initially increase and then decreases as the number of turns increases from 4 to 6, as shown in Fig. 3.16.

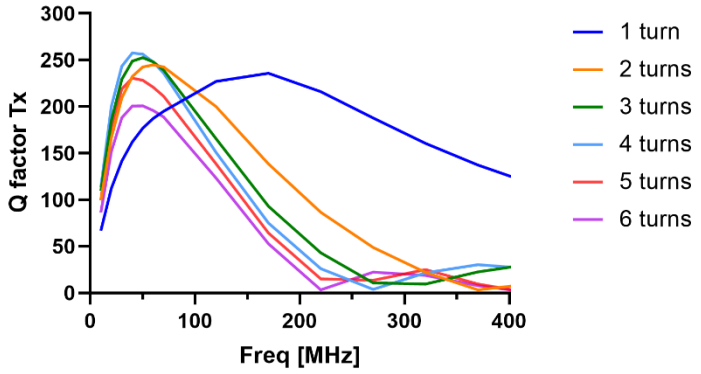

Figure 3.16:Tx Q factor varying turns (n_2=3 turns, w_2=0.12mm, s_2=0.08mm)

It can also be noted from Fig. 3.16 that the Q factor range is significantly higher than the Q factor values reported for the receiver. This is undoubtedly due to the larger size of the Tx compared to the Rx and the material used (copper), which presents better electromagnetic properties.

More predictable, on the other hand, is the value of the Q factor as the trace width of the coil increases. For higher values, the Q factor assumes greater values.

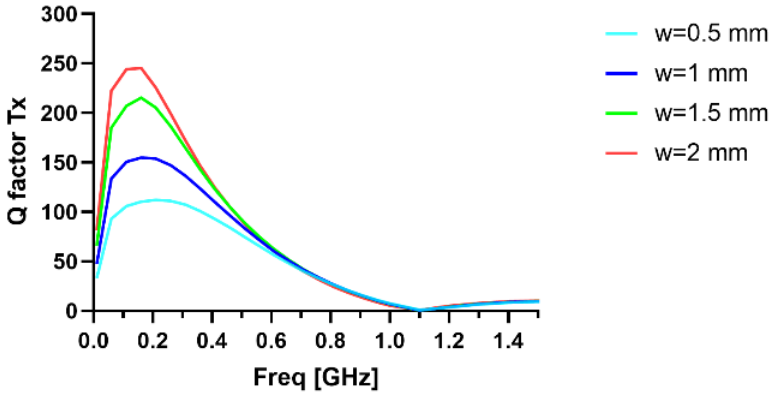

Figure 3.17:Tx Q factor varying width trace (n_1=5 turns, n_2=4 turns)

Same trend is observed for the correlation between the increase in the radius of the transmitter and the value of the Q factor with the remaining geometrical parameters of the coil unchanged. The behaviour is not strictly linear as can be seen in Fig. 3.18 and a variation of the frequency at which the maximum Q factor is obtained is also observable.

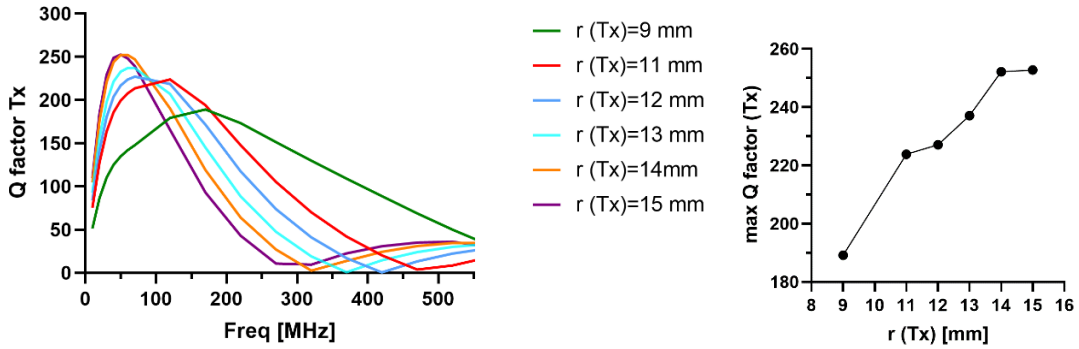

Figure 3.18: Tx Q factor varying Tx radius (n_1=5 turns, n_2=3 turns)

Proceeding to evaluate the parameters related to the electromagnetic coupling between transmitter and receiver, it can be seen how the number of turns of the transmitter affect the system's PTE and PDL results. Higher values of PTE and PDL are observed for the number of Tx turns in the average of those tested (3 and 4 turns) and are approximately 0.4% for PTE and 2 mW for PDL.

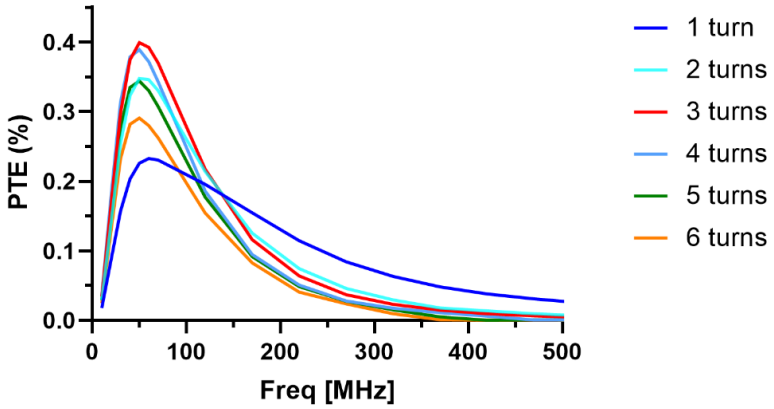

Figure 3.19: PTE varying Tx turns

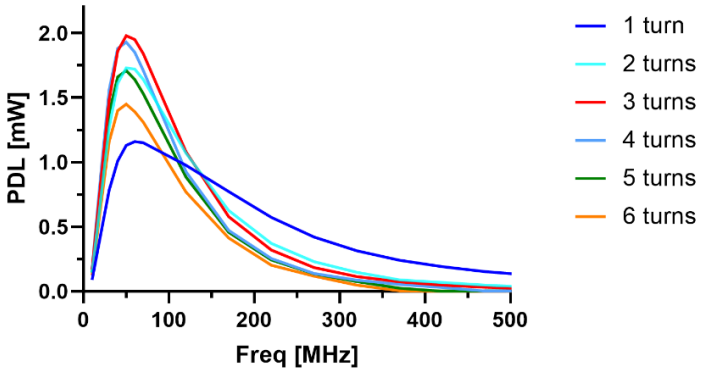

Figure 3.20: PDL varying Tx turns

3.3.2 Tx and Rx results - in tissues

The simulation concerning the coupling of the transmitter and receiver in the tissues is the one that allows us to build the complete simulation model to test the feasibility study of the IPT system. In this regard, as already discussed, the inductive coils (Tx and Rx) were optimised using the algorithm described in section 3.1 Fig. 3.5 [48] and consisting of several steps.

The algorithm involves analysing the geometrical parameters of the coil considering the constraints defined in step 1 and starting from the initial values selected in step 2 (section 3.1).

Regarding the third step of the optimisation algorithm, concerning the receiver, a representative graph which was evaluated is shown in the Fig. 3.21. Indeed, the value of n_2 (number of turns of the receiver) was chosen by displaying, as indicated by the algorithm, the value of the Q factor of the Rx as the number of turns of the Rx varies, and then selecting the number of turns that would return the maximum Q factor. In the figure, in our case this corresponded to 3 turns.

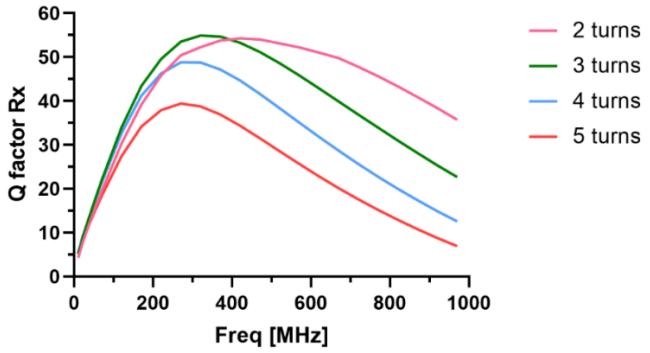

Figure 3.21: Example of simulation step 3.1 algorithm - Rx Q factor varying n_2

Having obtained the optimised design for the receiver, the steps dedicated to transmitter optimisation are performed. The results of one of the steps of this algorithm (step 4.3), in which the width trace value of the Tx is chosen according to the PTE maximisation, can be observed in Fig. 3.22.

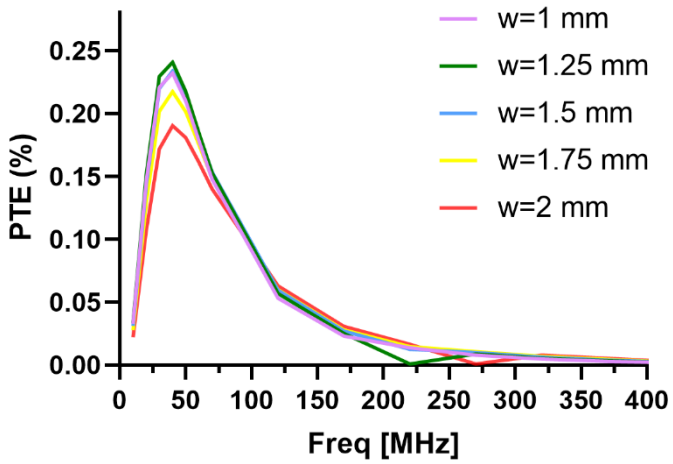

Figure 3.22: Example of simulation step 4.3 algorithm – PTE varying w_1

Finally, the last system parameter to be selected is the distance between the outer skin layer and the transmitter. It can be seen that as the distance increases, there is a decrease in the PTE value (Fig. 3.23) appearing as a fundamental parameter. In particular, for a distance of 1 mm, the PTE value achieved is close to 0.24%.

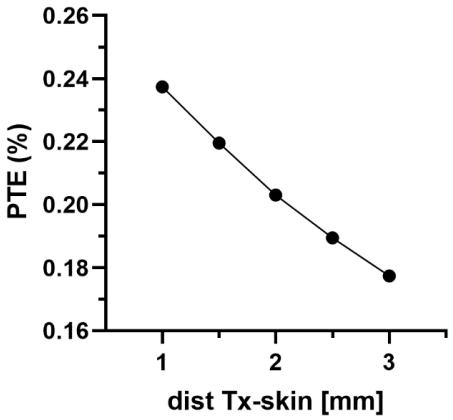

Figure 3.23:Simulation step 5 algorithm – PTE varying distance Tx-skin

3.3.2.1 Optimized design

I I n conclusion, following the algorithm steps, the optimised design resulted to be:

- For the transmitter (Tx):

Optimised design Transmitter	
n_1: number of turns (Tx)	4 turns
D_{o1}: outer diameter (Tx)	30 mm
w_1: width trace (Tx)	1.25 mm
s_1: gap inter turns (Tx)	0.75 mm

Table 3.9: Optimised Tx design parameters

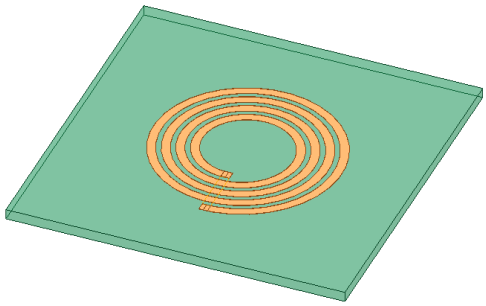

Figure 3.24:Optimised Tx design model

- For the receiver (RX):

Optimised design Receiver	
n_2: number of turns (Rx)	3 turns
D_{o2}: outer diameter (Rx)	3.36 mm
w_2: width trace (Rx)	0.180 mm
s_2: gap inter turns (Rx)	0.08 mm

Table 3.10: Optimised Rx design parameters

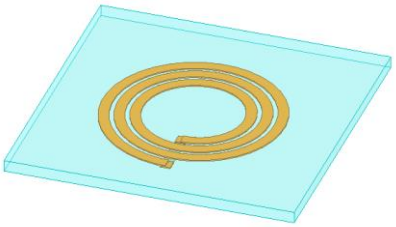

Figure 3.25: Optimised Rx design model

- Distance Tx-skin: 1 mm

Evaluating the results for PTE and PDL, the maximum values were reached for a frequency of 40 MHz as shown in Fig. 3.26 and Fig. 3.27 and were 0.24% for PTE, and 1.21 mW for PDL, showing a promising result for wirelessly transfer power.

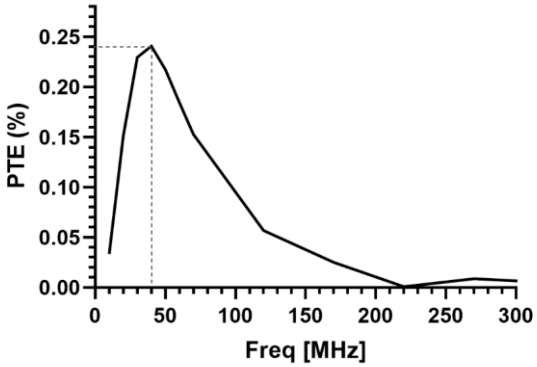

Figure 3.26: PTE at f=40MHz

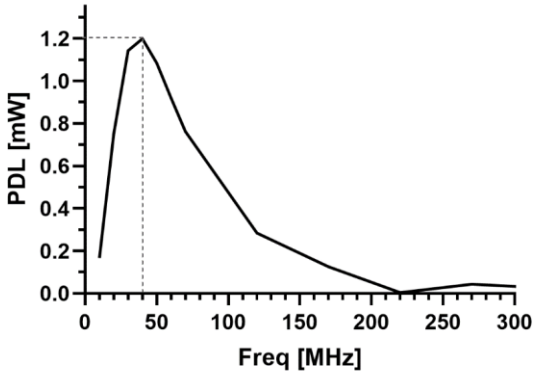

Figure 3.27: PDL at f=40MHz

The SAR value for a 40MHz frequency and for the optimised system obtained was also evaluated. The highest value observed was 0.208 W/kg (Fig. 3.28) and proved to be within regulatory limits and therefore safe [44].

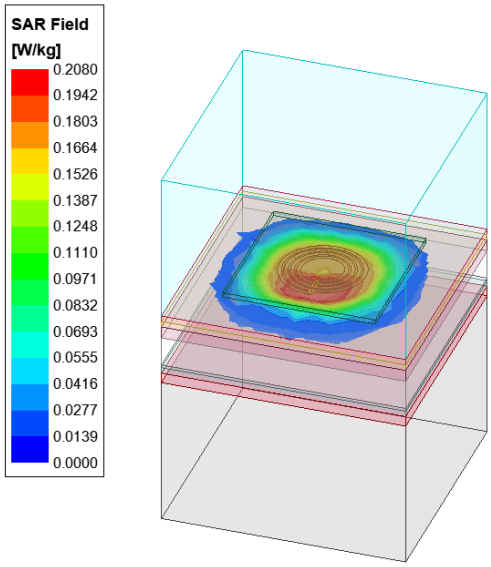

Figure 3.28: SAR values at f= 40MHz

3.3.2.2 Optimised design – lower Rx thicknesses

The fabrication method under test, based on the use of an evaporator to deposit magnesium, allows for further miniaturisation of the coil, resulting in thicknesses of less (for the deposition time chosen) than 2 µm

Evaluating the coupling parameters between Tx and Rx in the case where receiver thickness values from 1 to 2 µm were used, the following results were obtained.

Regarding the PTE, it exhibits for the tested values an increase with increasing thickness (Fig. 3.29) and the value for 1 µm equals 0,012%.

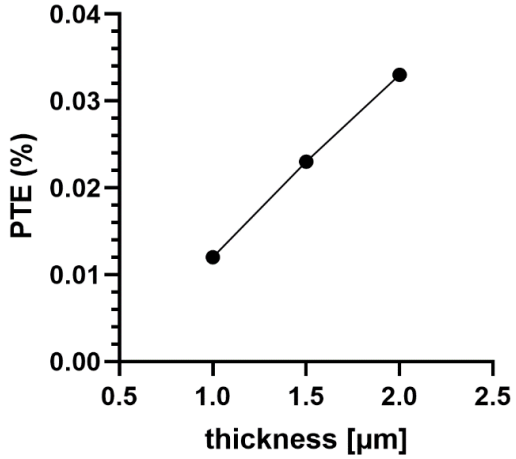

Figure 3.29: Max PTE value varying thickness

The PDL, whose value tends to increase as the thickness tested increases, presents same trend and for the minimum value of 1 µm it assumes a value of 0,061 mW (Fig. 3.30).

Overall, the results obtained suggest that it is possible to transfer power wirelessly even with reduced thicknesses.

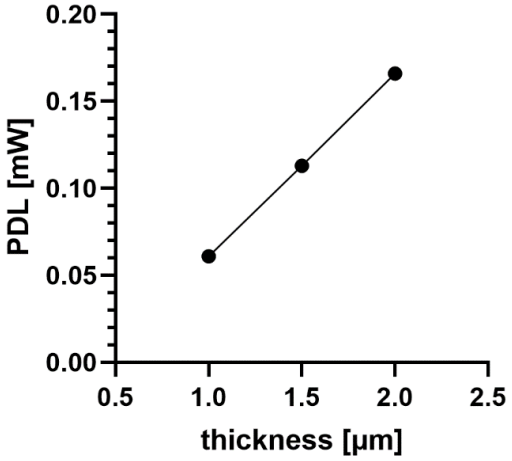

Figure 3.30: Max PDL value varying thickness

3.4 Literature comparison

The results obtained were compared with results found in the literature on optimisation and manufacturing studies of IPT systems.

			Literature references						
			[43]	[49]	[48]	[50]	[51]	[52]	Project
TX Design	outer diameter (mm)	**D1**	24	52	28	20	15	15	30
	wire width trace (mm)	**w1**	1	0,035	0,622	2	3	3	1.25
	number of turns	**n1**	1	24	5	1	1	1	4
	shape		hexagonal planar spiral coil	printed circuit board	wire-wound coil (AWG14)	side square loop	hexagonal loop	hexagonal loop	Printed Spiral coil
RX Design	outer diameter (mm)	**D2**	1	10	1	2	1	6,5	3.36
	wire width (mm)	**w2**	0,08	5	0,1	0,2	0,05	0,7	0.180
	number of turns	**n2**	7	8	7	1	1	1	3
	shape		wire-wound coil	hand wound coil (30AWG)	wire-wound coil (AWG24)	square loop	squared single loop	single loop	Printed Spiral coil
	Materials		copper, copper	copper, copper	copper, copper	copper, copper	copper, copper	copper, copper	copper, magnesium
	PTE	**η**	0,44% * 0,224 *	0,22% 50	1.86%* / 2.1* / 2.2	0,10% 0,15	0,05% 0,041	2,80% 0,8	0.24%* 1.21*
	PDL (mW)	**fp**	200	6,78	20	1000	400	300	40
Freq	operation frequency (MHz)		12	15	12	30	16	16	23.74
dist TX-RX	coupling distance (mm)	**d12**	5k	200	250	5,6	/	/	50
RI	load resistance (Ω)								

Table 3.11: Literature – project comparison

* =simulated

Each column of this table represents a literature work that has been chosen due to the comparable miniaturised dimensions of the employed receiver.

In [43], the results obtained in terms of PTE are close to the values obtained in the project design. Regarding the diameter of the transmitter, it is comparable, with a single turn, as are the number of turns and the geometrical parameters of the receiver. The small size of the receiver affects the PDL value, which is lower than the value obtained in the project in consideration. The high number of receiver turns, the WWC geometry and the transmitter diameter, however, make it possible to obtain a PTE comparable to the value obtained in the project.

The works presenting the greatest deviation are [48] and [52]. When analysing the geometrical parameters of the systems and comparing them with the design values, the higher PTE results are due to different causes. In the case of [48], both coils have WWC geometries and, although the receiver diameter is smaller, the number of turns, which positively influences the PTE as well as the PDL, is more than twice as high. In contrast, in the case of the work [52], the diameter of the receiver is larger than the receiver used in the project, as is the width trace, which leads to higher PTE results.

Comparable PTE values are presented in the work [49]. Although the coil diameter and number of turns are larger, the geometry of the transmitter and the narrow width trace lead to comparable PTE values. With regard to the PDL value, however, the higher geometrical characteristics in the receiver compared to the design receiver are reflected in the higher value.

In the remaining works,[50] and [51], the performances are lower than in the project. This, when comparing the geometric values of the transmitter and receiver, as well as for work [50], the distance between the two, is in line with what is expected.

In addition, the materials used must be taken into account. In literature, receiving coils are manufactured in copper, whereas in the case of the project under consideration, the material used to manufacture the receiving coil is magnesium. The two materials have different electromagnetic characteristics, even if only in terms of the electrical resistivity value, which is almost three times higher in magnesium than in copper.

Despite the challenges in terms of materials and miniaturisation, the feasibility study showed that the development of this optimised system leads to very promising results for wireless energy transfer.

4. Fabrication process

Once the optimal design for the inductive link between the Tx and Rx had been found in simulations, the next step was to proceed with the fabrication of the implantable receiver, which was developed using transient materials (magnesium and PCL), as suggested in the literature [53].

A coil fabrication technique has already been proposed in a previous work using laser cutter on a magnesium foil [1]. In this work, an alternative method for fabrication via evaporation of Mg is proposed in order to evaluate a fabrication method that would allow the device to acquire a further miniaturisation. The fabrication process is developed in a laboratory and clean room environment to ensure minimal contamination.

The process involves the development, on a PCL layer, of, first, the main spiral of the coil ("Mg spiral" in Fig. 4.1). At the center of the spiral, the trace width is enlarged to provide a contact point for the trace representing the other extremity of the coil, called "L-electrode" ("Mg L-electrode" in Fig. 4.1). Before proceeding to the deposition of the L-shaped part, an interlayer of PCL is interposed over the spiral, to cover and insulate its turns and leaving an opening at the location of the contact point in the center. Once the turns are in this way insulated, the L-shaped electrode is deposited by evaporation. Following the development of the second part of the connection, Au contact pads are sputtered at the extremities of the coil.

Finally, a final layer of PCL is overlaid to encapsulate the device.

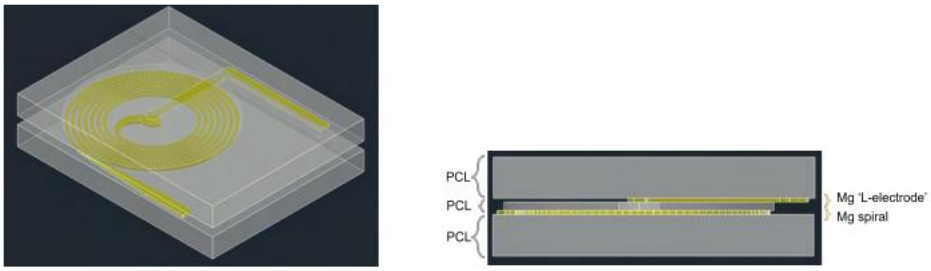

Figure 4.1: Final Rx coil model[1]

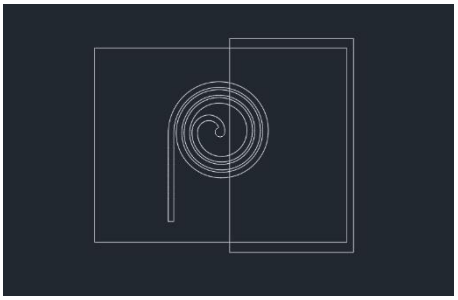

Figure 4.2: Interlayer view

4.1 Materials and methods

For the realization of the substrate:

- 4-inch glass wafer
- Polydimethylsiloxane: PDMS (Sylgard 184, 10:1 prepolymer:curing agent)

For the realization of the encapsulation layer:

- 4-inch Si wafer
- Polystyrene sulfonate: PSS (18 wt% in H2O, Sigma Aldrich)
- Chloroform (C2432, Sigma-Aldrich)
- Poly-ε-caprolactone: PCL (MW 50000, 25090, Polyscience, Inc.)

For the realization of the masks:

- 4-inch Si wafer
- Polyethylene terephthalate (PET) foil
- Polyimide (PI2611, Hitachi Chemical DuPont MicroSystems GmbH)
- Photoresist (AZ10XT, Microchemicals)

For the realization of the bioresorbable conductive coil:

- Titanium: Ti
- Magnesium: Mg

For the realization of contact pads:

- Gold: Au

4.1.1 Support layer

The manufacture of the Rx coil follows several processes and steps through the use of laboratory equipment. In order to make the device easy to handle, a glass wafer was used as a substrate which, in view of its transparency, also allows certain processes to be managed visually. The different layers for the receiver manufacture are stacked on top of each other and it was therefore necessary to use a layer of material on the glass wafer that would allow the different layers to adhere to the substrate. It was decided to use a 100 μm layer of polydimethylsiloxane (PDMS) which, due to its sticky behavior, guarantees the adhesion of the device.

The PDMS solution was made under chemical hood inside the clean room, mixing the base polymer with the curing agent at a ratio of 9:1. After mixing and degassing the solution in an automatic mixer (Thinky, USA), a portion was poured onto the glass wafer and spin coated at 660 rpm for 30s to achieve the desired thickness. Then the PDMS-coated glass wafer was baked in an oven at 75 ° C for 2 hours. In Fig. 4.3 the employment as support layer is shown.

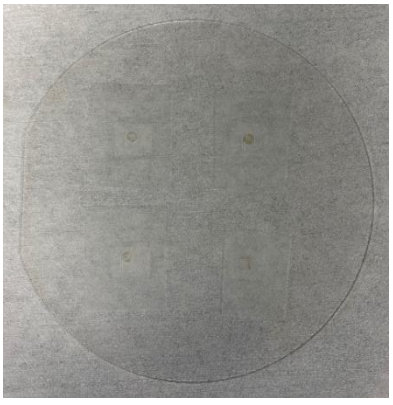

Figure 4.3: PDMS-coated glass wafer with PCL layers and coil's designs masks on before proceeding with the Ti sputter and Mg evaporation

4.1.2 PCL layer

The conductive part of the receiver coil must be encapsulated in a transient and biocompatible material, in this case poly-ε-caprolactone (PCL). In order to realise the PCL layers, first a release layer of PSS is spin coated on a 4-inch Si wafer and then baked at 145 °C for 10 minutes.

The PCL solution is obtained dissolving PCL (MW 50000, 25090, Polyscience, Inc.) in chloroform (C2432, Sigma-Aldrich) at a proportion of 30% w/v at 50°C for 2 hours. The PCL solution is then spin coated onto the PSS-coated wafer at 800 rpm. To remove residual stresses caused by the spin coating, a soft bake for 30 min at 75 °C was performed. This is followed by solvent evaporation by leaving the wafer under a chemical hood at room temperature for 1h. After complete solvent evaporation, the PCL layer was shaped into rectangles of size 10 x 8,5 mm and then detached from the wafer, by immersion in deionized (DI) water (dissolving the PSS release layer). The resulting PCL rectangles were dried and then placed on the PDMS-coated glass wafer.

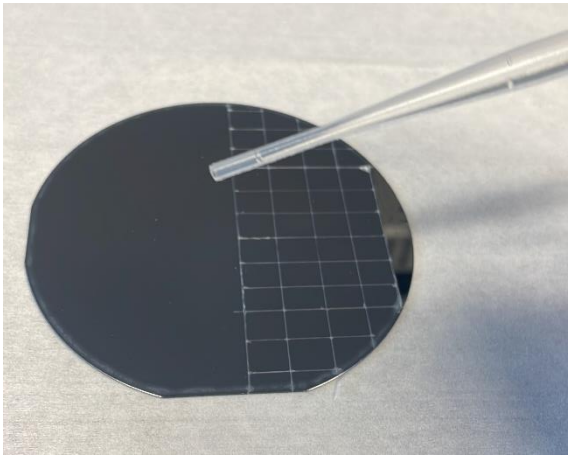

Figure 4.4: PCL rectangles releasing with DI

4.1.3 Mask fabrication

In order to deposit the materials that compose the coil, it is necessary to create a patterning mask. Three mask shapes have been fabricated: spiral (for the first and main part of the coil), L-electrode (to create the second extremity of the coil) and rectangular openings (to create the AU contact pads at the coil extremities).

In this regard, 2 different mask materials and thicknesses were tested:

4.1.3.1 PET mask

A 50 µm thick Polyethylene terephthalate (PET) foil was used, which was laser cutted (Excimer laser, OPTEC LSV3 Z18). The device used is a removal laser (Fig. 4.5), which requires the associated software to provide a CAD design that only marks the centre line that the laser remove beam will follow (Fig. 4.6).

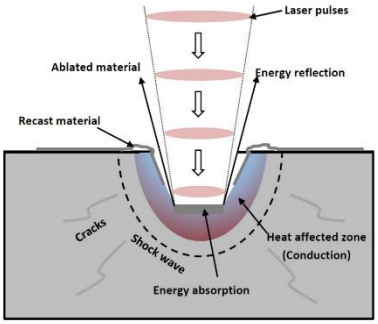

Figure 4.5:Excimer laser operation scheme [54]

For the cutting of PET, due to limitations of the equipment, large beam measurements are usually used as it is easier to obtain more accurate results. In our case therefore it was decided to use a circle beam shape **(**Demag 10x) of 196 µm diameter. In the case of the coil, the CAD design was realised to obtain a trace width of 196 µm and a gap between traces of 80 µm. The contact pads were designed as squares of 2 x 2 mm size.

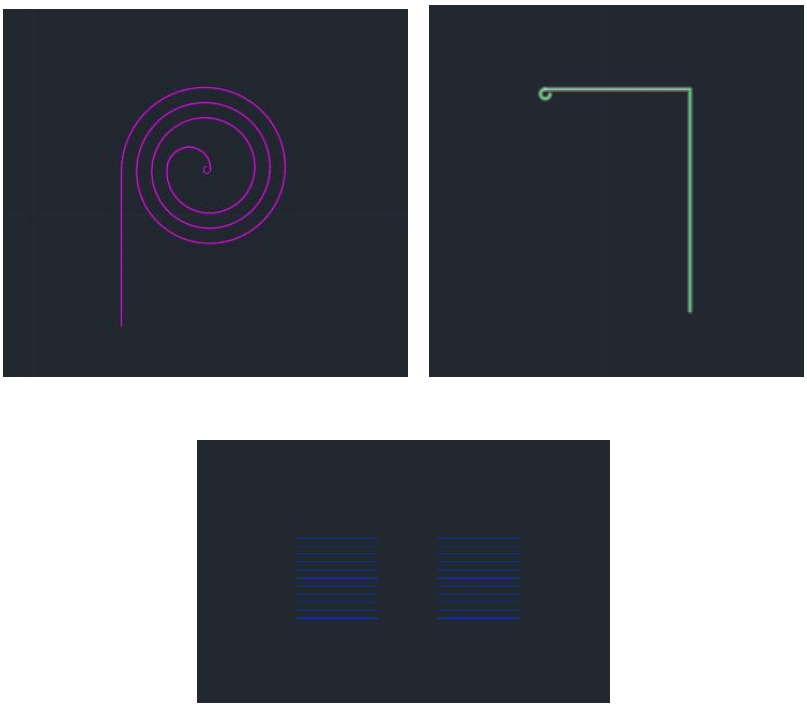

Figure 4.6: PET masks CAD design (coil: upper left, connection: upper right, contact pads: bottom)

4.1.3.2 PI mask

To develop the PI mask a Si wafer is used previously treated with a surface priming O_2 plasma (Pink, Germany) at 600 W for 2 minutes.

PI has been spun coated on the Si wafer, obtaining a thickness of 12 μm. The coated wafer is then placed on an hotplate at 80 ºC for 3 minutes and then at 110 ºC for 3 minutes and then subjected to a gradual hard bake treatment overnight: two steps of bake with increasing in temperature under different atmospheres (normal and N_2 atmosphere), interspersed with 1h baking at 200°C under N_2 atmosphere.

After a dehydration for 5 minutes at 110 ºC, a positive photoresist is spin coated obtaining a thickness of 12 μm.

The wafer is exposed to MLA 150 machine (Heidelberg Instruments) which uses a 405 nm laser to obtain a mask-less exposition reproducing the uploaded CAD design (Fig. 4.7).

The photoresist has been developed by AZ 726 MIF and then the uncoated PI has been etched, leaving the PI mask with the desired pattern.

The tested width measure is 180 μm and for the coil a space gap of 80 μm, reflecting the optimized design obtained in simulations.

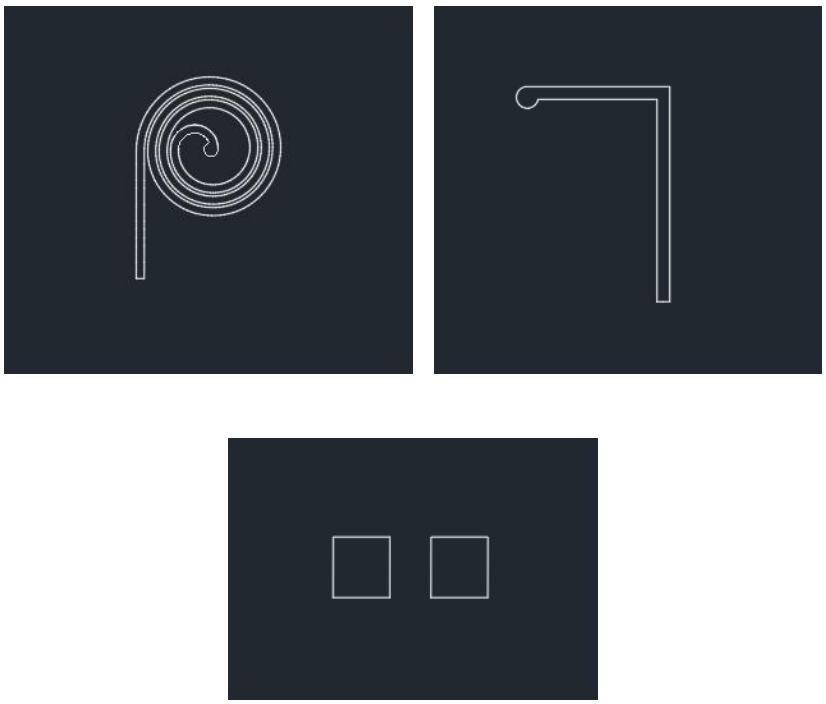

Figure 4.7: PI masks CAD design (coil: upper left, connection: upper right, contact pads: bottom)

In both cases, when the masks are created, they are lifted from the Si wafer and cut so that they cover a larger area than the PCL rectangles created previously. In this way, when manually overlaid onto the PCL layers, the masks touch the PDMS layer laterally, which, due to its sticky behaviour, aids in the adhesion of the masks to the substrate by not allowing movement.

In order to further improve adhesion between the PCL and the mask, the ensemble is put in a vacuum machine (EasyVac Pro, Solis) for improving the contact between the layers of the stack and reducing the amount of air between them. Then it is placed on a hotplate at 60 °C to allow the PCL to slightly melt and thus adhere to the mask. The melting time is short (10-20 s) and can be visually observed by looking at the PCL: it normally has a slightly white colour and when it starts to melt it becomes more transparent and must then be removed from the hotplate. The layers are kept in position during the melting with a PET foil.

Once removed from the hotplate, the PCL recovers its slightly white colour, and the masks are further fixed to the PDMS using tape.

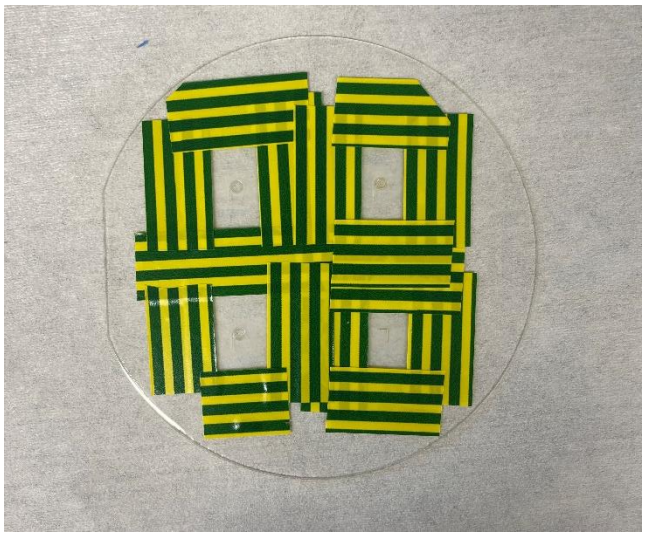

Figure 4.8: Fixed masks on PDMS-coated glass wafer and PCL

4.1.4 Conductive material deposition: Ti sputter

Once the mask is placed on the substrate, the deposition of the conductive parts is performed.

Initially, the wafers with the overlapping masks are placed inside the AC450 sputtering machine (Alliance Concept, FR) to deposit a 20 nm layer of Ti, which enables an improved adhesion of the Mg in the next step. Indeed, in the absence of the Ti layer, the quality of deposition decreases dramatically [1].

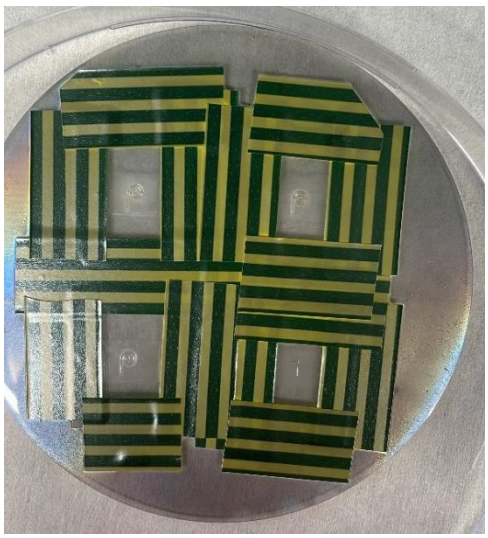

Figure 4.9: Wafer after the 20 nm Ti sputter

4.1.5 Conductive material deposition: Magnesium evaporation

Following Ti sputtering, the whole wafer is inserted into the EVA 300 vacuum evaporation machine (Alliance Concept, FR), (Fig. 4.10), for the deposition of magnesium (Mg).

Figure 4.10: EVA 300 vacuum evaporation machine

The chosen deposition time was 10 minutes, in order to avoid melting of the PCL layer during the process, in a pressure environment of 2,3 $\cdot 10^{-5}$ mBar. In addition, the measurement of the deposed magnesium was then carried out on the surface of an empty wafer inserted in the evaporator at the same time and using a profilometer (DektakXT) to verify the thickness of the deposited material with the evaporation time used. This measurement was carried out on a wafer that did not present the structures and not directly on the PCL sample as this allows to perform the measurements without deteriorating the sample. The measurement on PCL would have been critical as the deposited material presents a thin and fragile trace, which could therefore break if subjected to pressure from the tip used in the profilometer. Moreover, for the use of the device it is necessary to expose the magnesium trace to air, which would lead to oxidation of the magnesium.

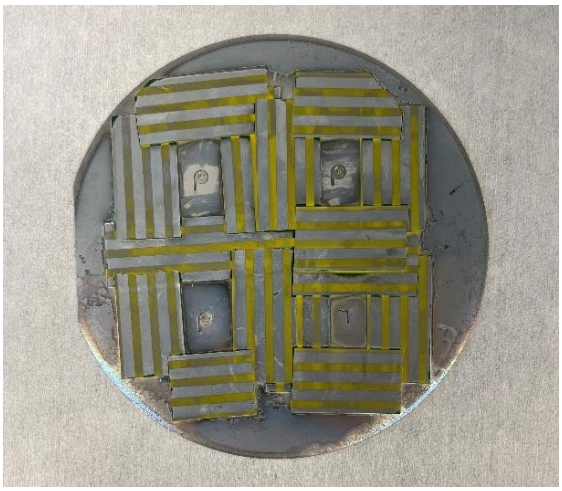

Figure 4.11: Wafer after the 10 minutes Mg evaporation (zoom on coil design: right)

4.1.6 Interlayer and Au sputter (centre connection area)

Following the deposition of the conductive material, the masks are gently removed, and a piece of PCL interlayer is inserted manually to proceed with the deposition of the material for the connection design (L-shaped design). Once the layer of PCL that will serve as the interlayer was positioned, it was adhered to the bottom layer of PCL by placing the wafer on a hotplate at 60°C for a few seconds (10s).

Subsequently, the height of the interlayer layer relative to the centre of the coil was measured using DektatXT to assess whether the upper layer (L-shaped design), once laid down, would not suffer bending and breakage due to the height difference to be bridged.

In order to limit the height difference, it was decided to proceed with Au sputter (AC450 sputtering machine, Alliance Concept, FR) in the central area where the contact between the 2 parts should occur. The mask used to delineate the areas where Au is to be deposited was fabricated following the same method used for the PI masks of the other designs and described in section 4.1.3.2.

The deposition rate for Au is 9 nm/min and thicknesses of 100 nm and then 15 nm were tested.

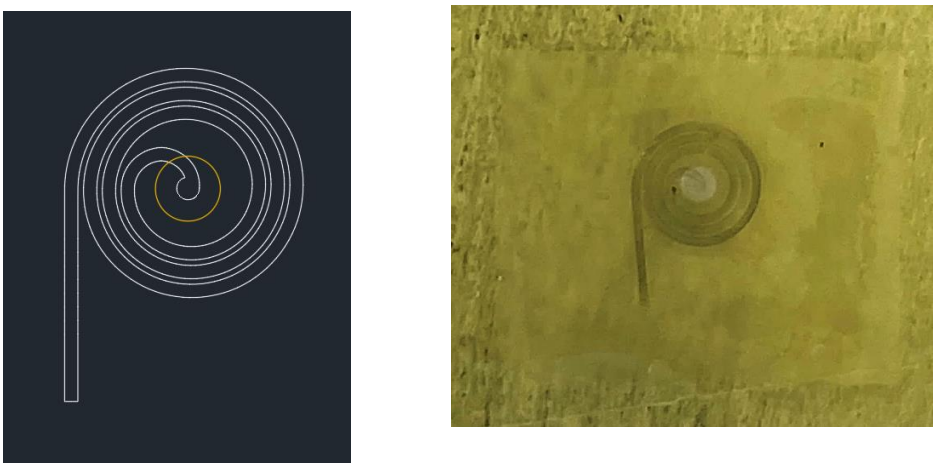

Figure 4.12: Connection area mask: CAD design on left, PI mask on PCL layer on right

4.1.7 Connection design and encapsulation

The mask was then positioned in order to proceed with the deposition of the L-shape connection. Fig. 4.13 shows the positioning of the mask, which was carried out following the same steps described in section 4.1.3.

Once the mask was positioned, the conductive material (Ti and Mg) was also deposited for this part, as described in paragraphs 4.1.4 and 4.1.5.

Finally, with the contact pads mask in place, a 15 nm gold sputter was applied in the same modality as described in the previous paragraph (4.1.6) using the contact pads design mask.

.

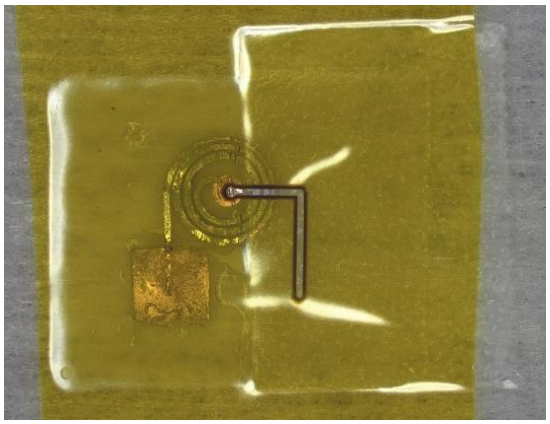

Figure 4.13: Connection design mask on PCL interlayer

4.2 Results and discussions

This fabrication method, as specified above, is an alternative to an already exploited method based on laser cutting of magnesium foil.

In general, the results obtained through this alternative fabrication method based on the evaporation of magnesium are mostly promising, although some adjustments and modifications must be made to improve this process.

4.2.1 Substrate and PCL layers

Concerning the fabrication of the PDMS substrate, the process is well structured and does not present any particular difficulties. Of course, one of the goals in this step is to limit the formation of micro bubbles as much as possible and thus make the substrate as homogeneous as possible.

The PCL layer, being part of the implanted device, certainly needs more care in its fabrication. Even in this case, the PCL mixture should be well homogenous and avoid bubbles in order to achieve uniformity of shape and behaviour.

4.2.2 Mask fabrication and Mg evaporation

The choice of mask materials and design required more care and attempts. As noted in the previous sections, a laser-cut PET mask was initially used to create the specific designs.

Fig. 4.14 shows the profile of the coil pattern created on a PET mask using the excimer laser.

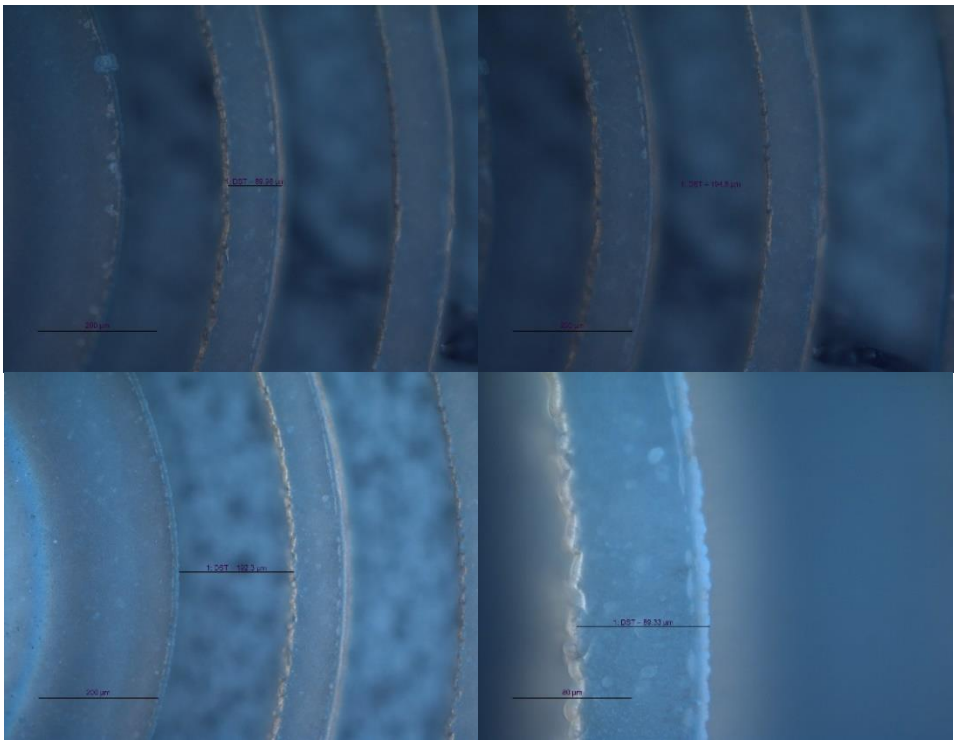

Figure 4.14: PET mask profiles

As it can be observed, the resulting mask presents rather jagged profiles and not as sharp as it would be expected, and the measurements obtained, determined through the microscope, do not reflect the design of the CAD. This is attributable to the laser cutting method which, as seen above, causes energy refraction waves and areas affected and deformed by heat. In particular, the measurements obtained under the microscope result in larger gap sizes than expected and, on the contrary, the mask sizes regarding the widths of the turns were smaller than the cut size examined, as it can be seen in the Table 4.1. The reason for this is probably to be found in the shape of the laser beam used, which tends to a U-shape when it encounters the material to be cut.

It was decided to use these masks anyway to evaluate the deposition of the conductive material and estimate the mask size and material deposition correlation, and so subsequently proceeded to sputter and evaporate Mg for coil design by overlaying this PET mask on the PCL.

The deposition results can be seen in Fig. 4.15.

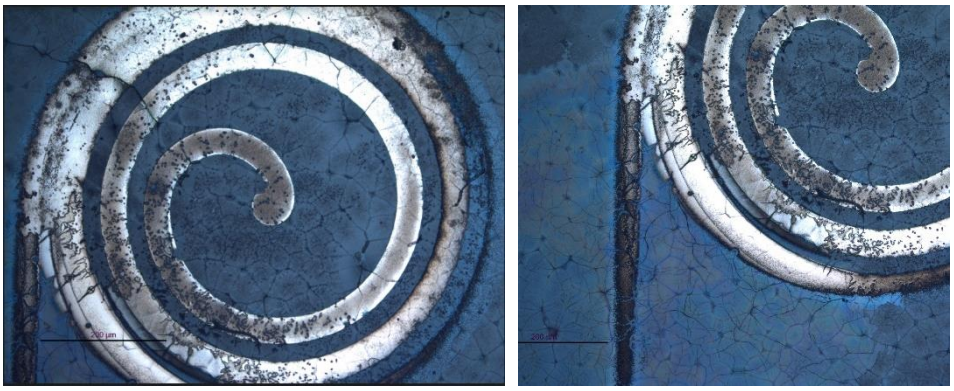

Figure 4.15: Mg deposition results with PET mask

It can be seen that the profiles of turns are undefined and often not present or overabundant to the extent that the gap between one turn and another cannot be formed.

The measurements of turns and gaps, when measurable, were far from the mask values as well as from the expected values.

	GAP (µm)					TURNS (µm)						
	SX			DX		SX				DX		
Mask	80.05	83.3	84.75	88.6	87.6	198.15	188.6	182.15	190.15	183.05	194.15	205.25
Deposition	104.06	113.83	/	119.47	118.9	174.97	173.33	200.05	/	159.57	152.8	164.6

Table 4.1: Comparison between PET mask measurements and obtained Mg deposition

In particular, as mentioned above for the mask, the measurements of the width of the turns obtained in the deposition are for the most part smaller than the desired dimensions and, on the contrary, for the gaps, measurements greater than those expected were obtained. The deviating values obtained from the deposition can be assumed to be due to the low adhesion of the mask to the PCL layer, which, as it does not adhere, lifts and leaves uncovered parts of the PCL where the magnesium is deposited, thus increasing the width of the turns or covering parts where the material fails to deposit. Also, the mask cut described above has to be considered as a critical factor, which tends to a u-shaped, non-uniform shape on the edges.

In order to overcome the problem of insufficient adhesion, it was decided to increase the period for which the wafer with the masks would remain on the hotplate and previously put the entire system under vacuum to eliminate air bubbles between the mask and substrate. As the sputtering and evaporation then proceeded, melting of the PCL on the PET mask occurred, which made it

difficult to extract the mask and, above all, produced holes in the substrate layer, which therefore became unusable (Fig. 4.16).

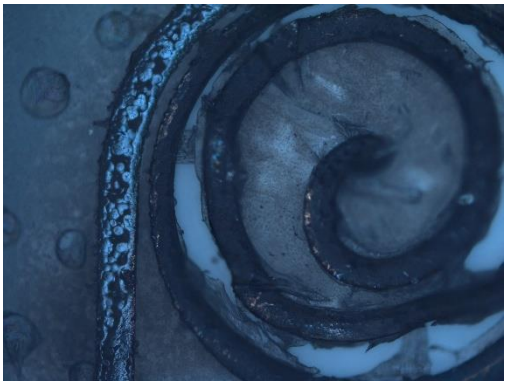

Figure 4.16: PCL layer degradation and breakage

It was then decided not to use this type of PET mask, but instead to proceed with another type of mask, which was produced using PI. The lithography and etching processes for the production of the mask, although delicate, led to the manufacture of a mask that, unlike the one made from PET, has sharp and precise contours (Fig. 4.17).

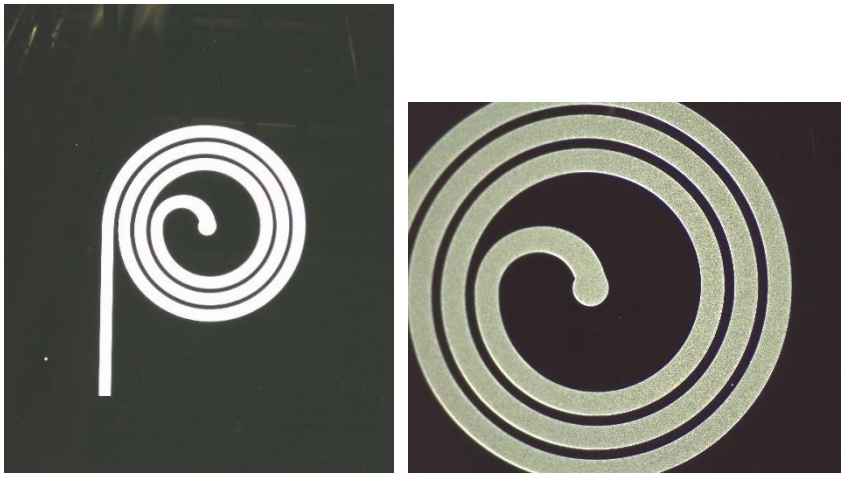

Figure 4.17: PI coil mask, zoom on the right

Using this type of mask, thanks to the use of the CAD file and the precision of the laser, we are therefore certain to obtain masks of accurate and desired dimensions.

However, one of the controversial aspects for this type of mask is the thickness of the PI layer produced.

While on the one side a thin layer allows for excellent adhesion with the PCL layer, as such a layer is also very flexible and adapts perfectly to the profile of the PCL (Fig. 4.18), on the other side it makes the PI layer slightly electrified and can make the handling of the mask difficult, especially for the spiral design. To overcome this, it is possible to intervene by lifting the mask from the Si wafer by placing a slightly DI-wet fabric on top, which thus avoids the problem and keeps the spiral shape intact.

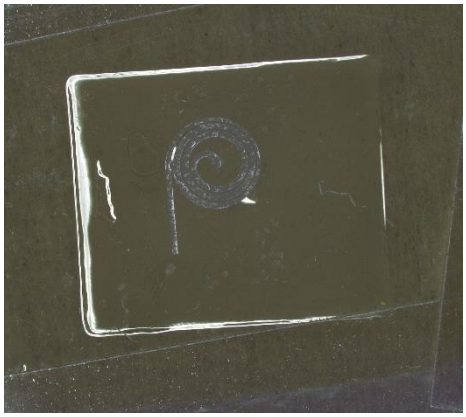

Figure 4.18: PI mask on PCL layer

Using this PI mask for magnesium deposition, an intact and well-defined coil was obtained as visible in Fig. 4.19.

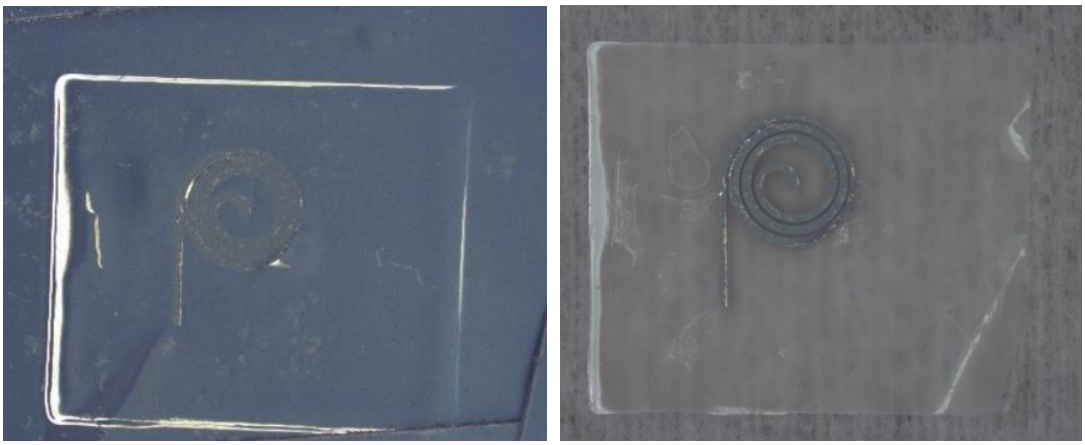

Figure 4.19:Coil design after Mg deposition: with PI mask on the left, PI mask removed on the right

An empty wafer was also placed inside the vacuum machine, at the same time as the wafer in which the coil fabrication masks had been placed, in order to test the thickness of magnesium that could be deposited in the chosen evaporation time.

The measurements taken on this wafer by means of a profilometer are expressed in Table 4.2 and it can be seen that all of them are in the range of 1.5 µm.

Position in wafer	Measure
North	1.5 µm
Middle	1.5 µm
South (outer diameter of the carousel)	1.2 µm
East	1.4 µm
West	1.5 µm

Table 4.2: 10 min Mg deposition measurements on wafer

4.2.3 Au sputter connection

For the realisation of the connection zones, Au sputter was performed.

Au sputtering with a thickness of 100nm was initially tried, and the result obtained can be seen in Fig. 4.20.

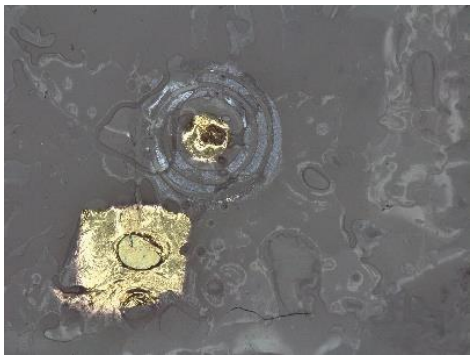

Figure 4.20: PCL layer and coil design after100nm Au sputter

It can be seen that the areas where Au has been sputtered present holes, which have penetrated the PCL layer, and the overall PCL layer appears to have bubbles, elevations and holes. The deterioration process of the PCL was probably due to the time on the hotplate to allow the mask

to adhere to the PCL layer, but also to the heat absorbed during time inside the sputter machine to enable the correct Au layer to be deposited.

Since the process of adhesion of the mask to the substrate could not be avoided, it was then decided to try other solutions

- A first solution was to adhere another identical layer of PCL underneath the PCL layer, thus creating a double layer that would better resist the heat inside the sputter and hence not cause holes. However, the attempt once on the hotplate to adhere the two layers led to a rapid melting of the top layer (Fig. 4.21), which probably became more heat sensitive.

Figure 4.21: Melted PCL layer

- A second solution concerns reducing the sputter time and thus obtaining a lower Au thickness. Specifically, an attempt was made with a thickness of 15 nm, thus reducing the sample stay within the sputter and achieving a result with minimal deterioration of the PCL layer and the device itself (Fig. 4.22).

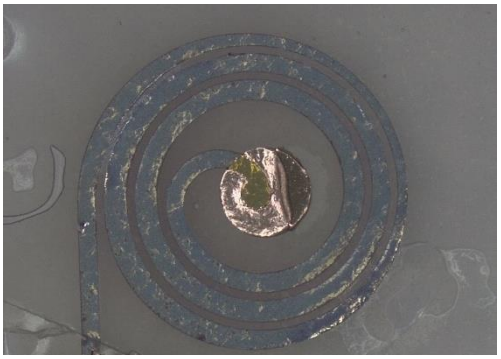

Figure 4.22: Connection area with 15nm Au sputter

4.2.4 Connection design and Au contact pads

Proceeding with the fabrication of the device, the interlayer and mask were placed for the L-shaped connection design and the conductive materials were evaporated.

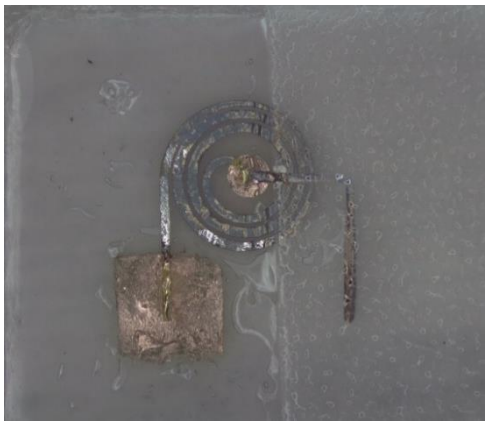

Figure 4.23: Device with interlayer and connection design

On this occasion, the magnesium was not deposited as expected.

In order to avoid subjecting the device obtained so far to temperature changes again and having to create the gold contact pads at the ends of the coil by using Au sputtering, the mask used to deposit the L-shape design was cut to leave the area of contact pad uncovered and the entire uncovered part (L-shaped design and contact pad) was sputtered with Au, leading to the result visible in Fig. 4.24.

Figure 4.24: Final device

Overall, the manufacturing results led to the complete fabrication of the device, which is congruent with what was expected to be produced although there was no resistance registered between the ends of the coil.

The probable reason for not detecting any electrical resistance in the coil could be due to a series of critical manufacturing steps. Possible reasons include the sensitivity of the PCL substrate to heat during the multiple manufacturing steps and the subsequent formation of holes, which could have interrupted the trace. In addition, the fragility of the magnesium trace itself could have caused the deposited material to deteriorate and break before measurement. The central connection between the two designs is also critical, and if not achieved correctly, could be the main cause of the unrecorded resistance.

5. Conclusions and future perspectives

5.1 Conclusions

The exploration of neural interfaces to meet patient needs is gaining more and more approval in the field of biomedical engineering and therapy. Endovascular devices require only a minimally invasive angioplasty surgery procedure to be implanted. Transient materials are used for the fabrication of the devices that can thus avoid the burden of a second surgery and reduce chronic inflammatory responses. wireless power transfer is a key strategy avoiding the use of a battery connected to the device via wires, which would be harmful causing negative immunological reactions.

The aim of this master's thesis is a feasibility study for a fully wireless and miniaturised neural interface using transient materials. Starting with the inductive elements of an IPT system, the coils, an attempt was first made to understand with software simulations the mechanisms of energy transport based on the principles of electromagnetism. Through the simulations, a design for the transmitter and receiver was obtained in order to achieve design optimisation in terms of power transfer. The transmitter final design consists of a copper 30 mm diameter coil with 4 turns, width trace of 1.25 mm and space gap of 0.75 mm. The optimal receiver in Mg was obtained instead with a design of 3 turns, width trace of 180 μm and space gap of 80 μm.

The PTE and PDL values obtained for this configuration resulted in 0.24% and 1.21mW respectively. Considering the small size and the material used for the receiver (magnesium), these results can be considered satisfactory and promising. In addition, in order to ensure safe use, the SAR value was evaluated, which, at a maximum of 0.208 W/kg, lies within the

standards. Furthermore, comparing these results with those of comparable IPT systems in the literature, they present themselves as valid for the development of a well-performing system.

With the intention of testing a receiver fabrication method based on magnesium evaporation, the coil design was tested for a thickness in the 1-2 μm range. The results for PTE and PDL were respectively 0,012% and 0,061 mW for the minimum thickness, thus demonstrating a feasibility in wirelessly transmitting power for this device.

The receiver coils, as part of a transient neural interface, are fabricated using transient materials: magnesium for the coil's traces and poly-ε-caprolactone as encapsulation. This new approach presents some limitations since the encapsulation layer is extremely sensitive to temperature increase and it melts during the coil's fabrication processes.

In conclusion, the evaporation-based process results an interesting procedure as a manufacturing method since it allows further miniaturisation of the device. However, the process is delicate, and the fabrication yield does not qualify as optimal for the development of this device and not fully appropriate. On the other hand, simulations confirm that it is possible to wirelessly transmit power to transient devices for minimally invasive implants.

5.2 Future improvements and perspectives

The feasibility study is the first step in order to consider integrating an IPT system in neural interfaces.

In this specific case, the study was started by carrying out simulations to quantify the expected results. The creation of a model faithful to the future in vivo application makes the results more reliable and allows the performance to be validated. Possible future improvements to be applied to the simulation could therefore consist of improving the model's faithfulness. In the case of the neural interface studied, endovascular, the coil Rx element, in vivo-like conditions inside the SSS, will be slightly bent following the profiles of the vessel in which it will be inserted and subjected to the pulsation of blood. It could therefore be considered to study in model under dynamic conditions and simulating the position of the Rx.

The fabrication method attempted for the receiver did not prove suitable for the production of the inductive element. The major limitation encountered was undoubtedly the sensitivity of the PCL to the high temperatures required by the fabrication process, which led to its degradation. It is therefore necessary to carry out further studies regarding the use of different materials alone or integrated with PCL. For example, copolymers with polylactic acid PLA and polyglycolic

acid (PGA) [55] could preserve the transient and biodegradable characteristics of PCL as well as the flexibility required for the implant. However, this study can represent a basis for future studies to promote solutions that could accommodate the use of the evaporator.

Other two elements for the fully wireless device are: a capacitor used as matching network; a diode capable of rectifying the generated signal and a smoothing output capacitor.the materials used for their manufacture must be in line with the purpose of the project and thus be biodegradable and transient.

For the diode, the most commonly used materials are metals and semiconductors such as magnesium (Mg), molybdenum (Mo), zinc-oxide (ZnO) and Si nanomembranes (Si NMs) [56][57][58]. Considering the problems encountered in the manufacture of the Rx coil, related to heat during the fabrication processes, an alternative to avoid these problems during the diode fabrication could be the use of polymers such as PEDOT:PSS. This type of polymer, although it is not a biodegradable material, it allows layers to be created through processes at room temperature such as spin coating.

Concerning the fabrication of the capacitor, it will consist of two metallic plates (magnesium) separated by a dielectric layer (i.e. SiO_2, MgO and Si_3N_4 [56]). Furthermore, in order to tailor the value of capacitance of this device, the thickness of the dielectric layer has to be taken into account.

In conclusion, focusing on the work that has been done, before proceeding with the realisation of the remaining circuit elements, further studies need to be carried out to handle the PCL-related limitations envisioning a final device to be characterised and compared with the simulations.

Bibliography

[1] F. A. B. G. L. Quaglia Filippo, “Design and fabrication of a biodegradable coil for inductive power transfer,” Politecnico di Torino, École Polytechnique Fédérale de Lausanne, 2022.

[2] L. Hochberg and T. Cochrane, “Implanted Neural Interfaces: Ethics in Treatment and Research,” in *Neuroethics in Practice*, Oxford University Press, 2013, pp. 235–250. doi: 10.1093/acprof:oso/9780195389784.003.0017.

[3] T. Kozai, “The History and Horizons of Microscale Neural Interfaces,” *Micromachines (Basel)*, vol. 9, no. 9, p. 445, Sep. 2018, doi: 10.3390/mi9090445.

[4] J. Wang, T. He, and C. Lee, “Development of neural interfaces and energy harvesters towards self-powered implantable systems for healthcare monitoring and rehabilitation purposes,” *Nano Energy*, vol. 65, p. 104039, Nov. 2019, doi: 10.1016/J.NANOEN.2019.104039.

[5] J. W. Hong, C. Yoon, K. Jo, J. H. Won, and S. Park, “Recent advances in recording and modulation technologies for next-generation neural interfaces,” *iScience*, vol. 24, no. 12, p. 103550, Dec. 2021, doi: 10.1016/J.ISCI.2021.103550.

[6] K. Kostarelos, M. Vincent, C. Hebert, and J. A. Garrido, “Graphene in the Design and Engineering of Next-Generation Neural Interfaces,” *Advanced Materials*, vol. 29, no. 42, p. 1700909, Nov. 2017, doi: 10.1002/adma.201700909.

[7] J. Kzhyshkowska, A. Gudima, V. Riabov, C. Dollinger, P. Lavalle, and N. Engin Vrana, “Macrophage responses to implants: prospects for personalized medicine,” 2015, doi: 10.1189/jlb.5VMR0415-166R.

[8] P. Stoeter, L. Dieterle, A. Meyer, and N. Prey, “Intracranial Electroencephalographic and Evoked-Potential Recording from Intravascular Guide Wires.”

[9] J. Boltze, D. B. Grayden, S. Giszter, S. A. Sheth, J. Z. Fan, and V. Lopez-Rivera, “Over the Horizon: The Present and Future of Endovascular Neural Recording and Stimulation,” 2020, doi: 10.3389/fnins.2020.00432.

[10] K. Yaeger and J. Mocco, “Future Directions of Endovascular Neurosurgery,” *Neurosurg Clin N Am*, vol. 33, no. 2, pp. 233–239, Apr. 2022, doi: 10.1016/J.NEC.2021.11.007.

[11] “https://synchron.com/.”

[12] S. E. John, D. B. Grayden, and T. Yanagisawa, “Expert Review of Medical Devices The future potential of the Stentrode,” 2019, doi: 10.1080/17434440.2019.1674139.

[13] A. Fanelli *et al.*, “Transient Neurovascular Interface for Minimally Invasive Neural Recording and Stimulation,” 2021, doi: 10.1002/admt.202100176.

[14] J. S. Shim, J. A. Rogers, and S. K. Kang, “Physically transient electronic materials and devices,” *Materials Science and Engineering: R: Reports*, vol. 145, p. 100624, Jul. 2021, doi: 10.1016/J.MSER.2021.100624.

[15] Y. Chen, “Transient electronics: Materials, mechanics, and applications.” [Online]. Available: https://lib.dr.iastate.edu/etd

[16] K. K. Fu, Z. Wang, J. Dai, M. Carter, and L. Hu, “Transient Electronics: Materials and Devices,” *Chemistry of Materials*, vol. 28, no. 11, pp. 3527–3539, Jun. 2016, doi: 10.1021/acs.chemmater.5b04931.

[17] W. B. Han, J. H. Lee, J. Shin, and S. Hwang, “Advanced Materials and Systems for Biodegradable, Transient Electronics,” *Advanced Materials*, vol. 32, no. 51, p. 2002211, Dec. 2020, doi: 10.1002/adma.202002211.

[18] A. Fanelli and D. Ghezzi, “Transient electronics: new opportunities for implantable neurotechnology,” *Curr Opin Biotechnol*, vol. 72, pp. 22–28, Dec. 2021, doi: 10.1016/J.COPBIO.2021.08.011.

[19] M. R. Major, V. W. Wong, E. R. Nelson, M. T. Longaker, and G. C. Gurtner, “The Foreign Body Response,” *Plast Reconstr Surg*, vol. 135, no. 5, pp. 1489–1498, May 2015, doi: 10.1097/PRS.0000000000001193.

[20] G. D. Cha, D. Kang, J. Lee, and D. Kim, “Bioresorbable Electronic Implants: History, Materials, Fabrication, Devices, and Clinical Applications,” *Adv Healthc Mater*, vol. 8, no. 11, p. 1801660, Jun. 2019, doi: 10.1002/adhm.201801660.

[21] M. D. B. Ahire, *Wireless Power Transfer System for Biomedical Application: A Review*.

[22] “https://www.circuitbread.com/ee-faq/how-does-wireless-power-transmission-work.”

[23] A. Abdolkhani, “Fundamentals of Inductively Coupled Wireless Power Transfer Systems,” in *Wireless Power Transfer - Fundamentals and Technologies*, InTech, 2016. doi: 10.5772/63013.

[24] “https://www.grandviewresearch.com/industry-analysis/wireless-charging-market.”

[25] T. Sun, X. Xie, and Z. Wang, *Wireless Power Transfer for Medical Microsystems*. New York, NY: Springer New York, 2013. doi: 10.1007/978-1-4614-7702-0.

[26] M. Etemadrezaei, "Wireless Power Transfer," *Power Electronics Handbook*, pp. 711–722, Jan. 2018, doi: 10.1016/B978-0-12-811407-0.00024-6.

[27] G. L. Barbruni, P. M. Ros, D. Demarchi, S. Carrara, and D. Ghezzi, "Miniaturised Wireless Power Transfer Systems for Neurostimulation: A Review," *IEEE Trans Biomed Circuits Syst*, vol. 14, no. 6, pp. 1160–1178, Dec. 2020, doi: 10.1109/TBCAS.2020.3038599.

[28] C. Dagdeviren *et al.*, "Transient, Biocompatible Electronics and Energy Harvesters Based on ZnO," *Small*, vol. 9, no. 20, pp. 3398–3404, Oct. 2013, doi: 10.1002/smll.201300146.

[29] Q. Guo *et al.*, "A Bioresorbable Magnetically Coupled System for Low-Frequency Wireless Power Transfer," *Adv Funct Mater*, vol. 29, no. 46, p. 1905451, Nov. 2019, doi: 10.1002/adfm.201905451.

[30] E. N. M. R. Sazonov, *Wearable Sensors: Fundamentals, Implementation and Applications.* 2014.

[31] A. Gopinath, "All About Transferring Power Wirelessly," *Electronics for You*, pp. 52–56, Aug. 2013.

[32] D. Xu, Q. Zhang, and X. Li, "Implantable Magnetic Resonance Wireless Power Transfer System Based on 3D Flexible Coils", doi: 10.3390/su12104149.

[33] "https://www.electronics-tutorials.ws/inductor/inductance.html."

[34] "https://www.electricaleasy.com/2016/08/skin-effect-and-proximity-effect.html."

[35] M. Schormans, V. Valente, and A. Demosthenous, "Practical Inductive Link Design for Biomedical Wireless Power Transfer: A Tutorial," *IEEE Trans Biomed Circuits Syst*, vol. 12, no. 5, pp. 1112–1130, Oct. 2018, doi: 10.1109/TBCAS.2018.2846020.

[36] T. Johansson, "TSEK03: Radio Frequency Integrated Circuits (RFIC) Lecture 7: Passive Devices."

[37] Uei-Ming Jow and M. Ghovanloo, "Modeling and optimization of printed spiral coils in air and muscle tissue environments," in *2009 Annual International Conference of the IEEE Engineering in Medicine and Biology Society*, Sep. 2009, pp. 6387–6390. doi: 10.1109/IEMBS.2009.5333876.

[38] P. Abiri, A. Yousefi, H. Cao, J.-C. Chiao, and T. K. Hsiai, “Wirelessly Powered Medical Implants via Radio Frequency,” in *Interfacing Bioelectronics and Biomedical Sensing*, Cham: Springer International Publishing, 2020, pp. 101–116. doi: 10.1007/978-3-030-34467-2_4.

[39] A. I. Kanaan and A. M.A. Sabaawi, “Implantable Wireless Systems: A Review of Potentials and Challenges,” in *Antenna Systems*, IntechOpen, 2022. doi: 10.5772/intechopen.99064.

[40] N. J. Jameson, M. H. Azarian, M. Pecht, K. Wang, and X. Aidong, “Electromagnetic coil equivalent circuit model sensitivity analysis for impedance-based insulation health monitoring,” in *2017 Prognostics and System Health Management Conference (PHM-Harbin)*, Jul. 2017, pp. 1–6. doi: 10.1109/PHM.2017.8079188.

[41] “https://www.electronics-tutorials.ws/inductor/mutual-inductance.html.”

[42] M. Kiani and M. Ghovanloo, “A figure-of-merit for design of high performance inductive power transmission links for implantable microelectronic devices,” in *2012 Annual International Conference of the IEEE Engineering in Medicine and Biology Society*, Aug. 2012, pp. 847–850. doi: 10.1109/EMBC.2012.6346064.

[43] D. Ahn and M. Ghovanloo, “Optimal Design of Wireless Power Transmission Links for Millimeter-Sized Biomedical Implants; Optimal Design of Wireless Power Transmission Links for Millimeter-Sized Biomedical Implants,” *IEEE Trans Biomed Circuits Syst*, vol. 10, no. 1, p. 125, 2016, doi: 10.1109/TBCAS.2014.2370794.

[44] “https://www.fcc.gov/consumers/guides/wireless-devices-and-health-concerns.”

[45] “https://www.itu.int/pub/R-REG-RR.”

[46] A. Ali, M. N. Mohd Yasin, M. Jusoh, N. A. M. Ahmad Hambali, and S. R. Abdul Rahim, “Optimization of wireless power transfer using artificial neural network: A review,” *Microw Opt Technol Lett*, vol. 62, no. 2, pp. 651–659, Feb. 2020, doi: 10.1002/mop.32089.

[47] R. Pagano, S. Abedinpour, A. Raciti, and S. Musumeci, “Efficiency optimization of an integrated wireless power transfer system by a genetic algorithm,” in *2016 IEEE Applied Power Electronics Conference and Exposition (APEC)*, Mar. 2016, pp. 3669–3676. doi: 10.1109/APEC.2016.7468398.

[48] A. Ibrahim and M. Kiani, “A Figure-of-Merit for Design and Optimization of Inductive Power Transmission Links for Millimeter-Sized Biomedical Implants,” *IEEE Trans*

Biomed Circuits Syst, vol. 10, no. 6, pp. 1100–1111, Dec. 2016, doi: 10.1109/TBCAS.2016.2515541.

[49] R. R. Harrison, "Designing Efficient Inductive Power Links for Implantable Devices," in *2007 IEEE International Symposium on Circuits and Systems*, May 2007, pp. 2080–2083. doi: 10.1109/ISCAS.2007.378508.

[50] A. S. Y. Poon, S. O'Driscoll, and T. H. Meng, "Optimal Frequency for Wireless Power Transmission Into Dispersive Tissue," *IEEE Trans Antennas Propag*, vol. 58, no. 5, pp. 1739–1750, May 2010, doi: 10.1109/TAP.2010.2044310.

[51] M. Mark, T. Björninen, L. Ukkonen, L. Sydänheimo, and J. M. Rabaey, *SAR Reduction and Link Optimization for mm-Size Remotely Powered Wireless Implants Using Segmented Loop Antennas*. 2011. doi: 10.1109/BIOWIRELESS.2011.5724339.

[52] R. Muller *et al.*, "A Minimally Invasive 64-Channel Wireless μECoG Implant; A Minimally Invasive 64-Channel Wireless μECoG Implant," *IEEE J Solid-State Circuits*, vol. 50, no. 1, 2015, doi: 10.1109/JSSC.2014.2364824.

[53] Q. Guo *et al.*, "FULL PAPER www.afm-journal.de A Bioresorbable Magnetically Coupled System for Low-Frequency Wireless Power Transfer," 2019, doi: 10.1002/adfm.201905451.

[54] "https://www.epfl.ch/research/facilities/cmi/equipment/packaging-miscellaneous/optec-lsv3/."

[55] C. Migliaresi, "Composites," *Biomaterials Science: An Introduction to Materials: Third Edition*, pp. 223–241, Jan. 2013, doi: 10.1016/B978-0-08-087780-8.00024-3.

[56] J. Koo and M. R. MacEwan, "Wireless bioresorbable electronic system enables sustained nonpharmacological neuroregenerative therapy", doi: 10.1038/s41591-018-0196-2.

[57] Y. S. Choi *et al.*, "Stretchable, dynamic covalent polymers for soft, long-lived bioresorbable electronic stimulators designed to facilitate neuromuscular regeneration," *Nat Commun*, vol. 11, no. 1, p. 5990, Dec. 2020, doi: 10.1038/s41467-020-19660-6.

[58] F. Seitz, "Fully implantable and bioresorbable cardiac pacemakers without leads or batteries", doi: 10.1038/s41587-021-00948-x.